VOLUME 20 NO. 1 | JANUARY 2026
P-ISSN: 1411-1616 | E-ISSN:2549-8215

# JURNAL ILMIAH BERKALA SAINS DAN TERAPAN KIMIA

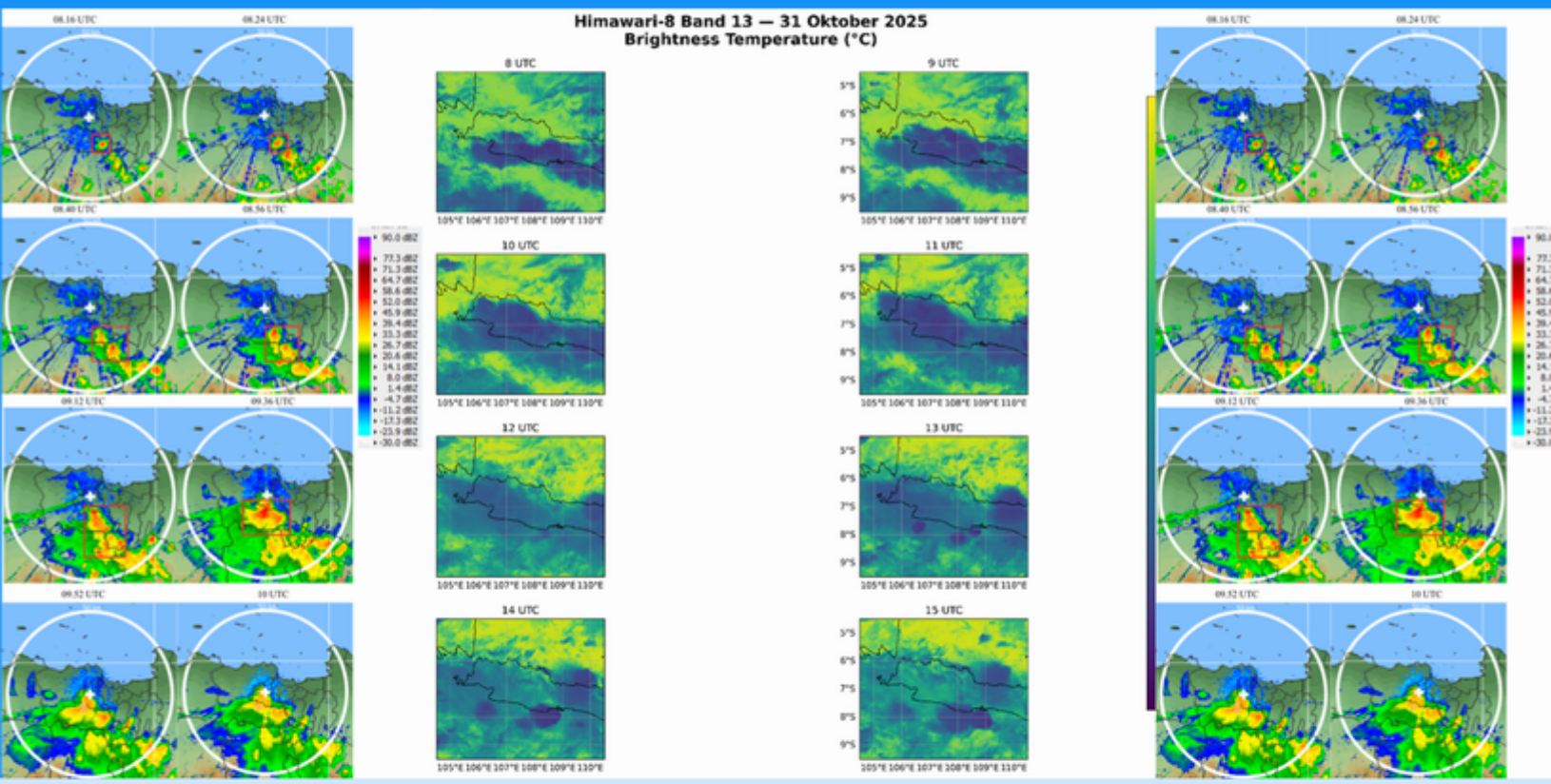


Tangerang Radar and Satellite Images (Prakoso *et al*, p. 30, 32)

JURNAL ILMIAH BERKALA SAINS DAN TERAPAN KIMIA

PUBLISHED BY:
CHEMISTRY DEPARTMENT, FACULTY OF MATHEMATICS AND NATURAL SCIENCES
LAMBUNG MANGKURAT UNIVERSITY, INDONESIA

**Jurnal Ilmiah Berkala: Sains dan Terapan Kimia**
*Vol. 20 No. 1, January 2026*

## *SUPERVISORY BOARD*

Head of Chemistry Department, Faculty of Mathematics and Natural Sciences, Lambung Mangkurat University

## *PUBLISHER*

Chemistry Department, Faculty of Mathematics and Natural Sciences, Lambung Mangkurat University

## *MAILING ADDRESS*

Jl. A. Yani Km. 36 Banjarbaru, Kalimantan Selatan , Indonesia 70714
Phone: 0511-4773112, 0511-4782899
Email: jstk@ulm.ac.id

## *FIRST EDITION: 2007*

## *EDITOR IN CHIEF*

Dr. Rahmat Eko Sanjaya, M.Si.

## *EDITORIAL BOARD*

***Managing Editor*** : Dyah Ayu Pramoda Wardani, M.Sc.

***Editorial Board Members:***

Prof. Dr. Gusrizal, S.Si., M.Si. (Universitas Tanjungpura, Pontianak)
Prof. Sunardi, S.Si., M.Sc., Ph.D. (Universitas Lambung Mangkurat, Banjarbaru)
Dr. RR. Dirgarini Julia Nurlianti Subagyono (Universitas Mulawarman, Samarinda)
Sura Menda Ginting, Ph.D. (Universitas Bengkulu, Bengkulu)
Yuana Nurulita,S.Si, M.Si, Ph.D (Universitas Riau, Riau)
Achmad Ramadhanna'il Rasjava, S.Si., M.Si. (Universitas Lambung Mangkurat)
Dahlena Ariyani, S.Si., M.S. (Universitas Lambung Mangkurat)
Dyah Ayu Pramoda Wardani, M.Sc. (Universitas Lambung Mangkurat)
Dr. Ahmad Budi Junaidi, M.Si. (Universitas Lambung Mangkurat)
Nawwal Hikmah, M.Sc. (Universitas Lambung Mangkurat)
Dr. Muddatstsir Idris, M.Si. (Universitas Lambung Mangkurat)
Utami Irawati, Ph.D. (Universitas Lambung Mangkurat)
Amalia Khairunnisa, M.Sc. (Universitas Lambung Mangkurat)
Aulia Rhamdani Arfan, M.Si. (Universitas Lambung Mangkurat)
Dr. Abdul Aji (Institut Teknologi Sumatera)
Fatiha Khairunnisa (Universitas Airlangga)
Herdayanto Sulistyo Putro (Institut Teknologi Sepuluh Nopember)
Ika Fitriani Juli Palupi (Politeknik Industri Logam Morowali)
Ir. Rendy Muhamad Iqbal, Ph.D. (Universitas Palangka Raya)

***Reviewer for this Issue***
***Jurnal Ilmiah Berkala Sains dan Terapan Kimia***
***Volume 20, Number 1, January 2026***

Dr. Umi Baroroh Lili Utami, M.Si. (Universitas Lambung Mangkurat)
Nawwal Hikah, S.Si., M.Si. (Universitas Lambung Mangkurat)
Dr. Rahmat Eko Sanjaya, M.Si., (Universitas Lambung Mangkurat)
Dahlena Ariyani, S.Si., MS. (Universitas Lambung Mangkurat)
Dyah Ayu Pramoda Wardani , M.Sc. (Universitas Lambung Mangkurat)
Dr. Muddatstsir Idris, M.Si. (Universitas Lambung Mangkurat)
Utami Irawati, Ph.D. (Universitas Lambung Mangkurat)
Tety Wahyuningsih Manurung, M.Si. (Universitas Palangka Raya)

## *SITE EDITOR AND ADMINISTRATOR*

Otok Pujinarko



## *ABOUT US*

(Jurnal Ilmiah Berkala) Sains dan Terapan Kimia publishes scientific articles in the Chemistry field which include, but not limited to, research in chemistry, theoretical chemistry, and applied chemistry. This journal also publishes review articles about the development of chemistry. All the articles in this journal will go through a peer-review process to ensure that the quality of the article meets our standard before being published. Each article submitted to our journal will be reviewed by a reviewer having the expertise in the field. Shall the article submitted is deemed acceptable to be published in our journal, it is the writer's responsibility to make the necessary change and revision as recommended by the reviewer.
This journal is open access journal which means that all content is freely available without charge to users or / institution. Users are allowed to read, download, copy, distribute, print, search, or link to full text articles in this journal without asking prior permission from the publisher or author.

**Sains dan Terapan Kimia** (Jurnal Ilmiah Berkala) is published twice a year on January and July. There is no fee for authors to submit their manuscripts to be considered for publication in this jurnal. When the article is accepted for the publication. The publication fee is IDR 350.000,00 that covers article processing and DOI processing charge. Payment should be made by bank transfer to this account below

Bank : BNI Banjarbaru
Account Number **107840008**
Account Name : Dahlena Ariyani

Please send a confirmation of your proof of payment to jstk@ulm.ac.id

# TABLE OF CONTENTS

**Characteristics of Chitosan from Chitin Deacetylation Using Different NaOH Concentration and Evaluation of Its Slubility in Liquid Smoke ……..1-11**
Ahmad Budi Junaidi*, Nurul Hikmah, Utami Irawati, Nawwal Hikmah, Taufiqur Rohman

**Network Pharmacology-Based Evaluation of Sungkai (Peronema canescens J.) Leaf Bioactive Compounds as Potential Therapeutics for Cervical Cancer ……..... 12-26**
Ratih Dyah Puspitasari*, Ahmad Sazali, and Indra Lasmana Tarigan

**Analysis of Atmospheric Vertical Structure During Hail in Tangerang: A Comparative Study of ECMWF Model Data and Radiosonde Observations.....27-36**
Dhanu Prakoso*, Aries Kristianto

**Performance Evaluation of Bentonite–Nano $SiO_2$ as an Adsorbent in the Decolorization Process of Rhodamine B.....37-45**
Regna Tri Jayanti, Miftahul Khairati, Enny Nurmalasari*, Puji Rahayu, Dennis Farina Nury, Okti Ulandari, Andhini Putri Trianita

**Efficiency of Chitosan and Alum as Coagulants for Peat Water Treatment.....46-57**
Utami Irawati*, Dahlena Ariyani, Taufiqur Rohman

JURNAL ILMIAH BERKALA SAINS DAN TERAPAN KIMIA

**Jurnal Ilmiah Berkala: Sains dan Terapan Kimia**
*Vol. 20 No. 1, January 2026*

# Characteristics of Chitosan from Chitin Deacetylation Using Different NaOH Concentration and Evaluation of Its Solubility in Liquid Smoke

# Karakteristik Kitosan Hasil Deasetilasi Kitin Cangkang Rajungan Menggunakan Konsentrasi NaOH Bervariasi Dan Uji Kelarutannya dalam Asap Cair

**Ahmad Budi Junaidi[1,2*)], Nurul Hikmah[1)], Utami Irawati[1)] Nawwal Hikmah[1)] Taufiqur Rohman[1)]**

[1]Departement of Chemistry, Faculty of Mathematics and Natural Sciences, Universitas Lambung Mangkurat, Jl. A. Yani Km 36, Banjarbaru 70714, Indonesia
[2]Biomaterials Laboratory, Faculty of Mathematics and Natural Sciences, Universitas Lambung Mangkurat, Jl. A. Yani Km 36, Banjarbaru 70714, Indonesia

*Email: abjunaidi@ulm.ac.id

## ABSTRACT

*This research aimed to determine the effect of chitosan characteristics produced from the deacetylation of chitin with various concentrations of NaOH on its solubility in liquid smoke. Chitin produced from rajungan shell raw materials was deacetylated using 40% NaOH (K40%), 50% (K50%), and 60% (K60%). The resulting chitosan was then measured of its degree of deacetylation (DD) with FTIR method, molecular weight (MW) with viscometry method, and solubility in liquid smoke was conducted qualitatively. The results showed that K40% had a DD of 56.99%, K50% had a DD of 72.86% and a BM of 149.1 kDa, also K60% had a DD of 82.87% and a BM of 102.6 kDa. The solubility of chitosan in 10% liquid smoke indicated that K40% was not dissolved, K50% was almost completely dissolved, and K60% was completely dissolved.*

**Keywords**: Chitin deacetylation; chitosan; liquid smoke; solubility.

**Received**: 06 January 2026 ; **Accepted**: 21 January 2026: **Available online**: 29 January 2026

## 1. INTRODUCTION

The primary sources of chitin and chitosan that have been widely utilized to date are the skins/shells of crustaceans (Saravanan, et al. 2023). Chitin is the second most abundant biopolymer in nature after cellulose. Despite its abundance, the utilization of chitin remains limited. One of the main reasons for this limited use is its insolubility in water, diluted acids, alkalis, and organic solvents. Therefore, the chemical structure of chitin is typically modified to obtain derivatives with improved chemical properties. One such derivative is chitosan. The modification of chitin into chitosan is achieved by converting the acetamide groups (–$NHCOCH_3$) in chitin into amine groups (–$NH_2$) through the removal of acetyl groups, a process known as

deacetylation (Aberoumand & Hoseinian, 2025).

The deacetylation of chitin to produce chitosan can be carried out using highly concentrated strong bases, with sodium hydroxide (NaOH) being the most used. According to Zuwanna, et al. (2025), the extent of acetyl group removal increases with increasing NaOH concentration; in other words, higher NaOH concentrations during the deacetylation process result in a higher degree of deacetylation. This increase is accompanied by a decrease in yield and molecular weight (Ghanem, et al., 2025).

Chitosan exhibits low solubility in neutral or alkaline water but readily dissolves in dilute weak acids with pH < 6, such as acetic acid, formic acid, and citric acid, due to its structural richness in amine groups ($–NH_2$). When chitosan is dissolved in weakly acidic media, the amine groups become protonated to form positively charged $–NH_3^+$ groups, rendering chitosan a cationic polyelectrolyte that is stably dispersed in aqueous media (Vo et al., 2025).

Liquid smoke contains organic acids, one of which is acetic acid. The presence of acetic acid makes liquid smoke a potential solvent for chitosan. This has been demonstrated by Junaidi et al. (2019) , who reported that liquid smoke at concentrations of 5–15% was capable of dissolving chitosan at concentrations exceeding 50 g/L. According to Wang and Roman (2023), the solubility of chitosan is strongly influenced by its characteristics, particularly the degree of deacetylation (DD) and molecular weight (MW). Chitosan characteristics such as DD, MW, antibacterial activity, and antioxidant properties are affected by the source of raw materials (shrimp shells, crab shells, fungi) and the preparation method (Niu & Hu, 2024). This study was conducted to determine the DD and MW characteristics of chitosan produced from the deacetylation of crab shell chitin using varying NaOH concentrations. In addition, the effect of the resulting chitosan characteristics on its solubility in liquid smoke was also investigated. This study aims to prove how much influence the concentration of NaOH used in the deacetylation process of crab shell chitin has on the DD and MW values and the solubility level of chitosan produced in liquid smoke.

## 2. MATERIALS AND METHODS

### *2.1. Materials*

This study was conducted at the Biomaterials Laboratory, Faculty of Mathematics and Natural Sciences, Universitas Lambung Mangkurat, Banjarbaru, and at the Organic Chemistry Laboratory, Faculty of Mathematics and Natural Sciences, Universitas Gadjah Mada. The materials used in this study included crab shells obtained from Sekandis Village, South Pamukan Subdistrict, Kotabaru Regency, liquid smoke derived from coconut shells with a phenol content of 2.22% GAE g/L and a total acid content of 14.52% AAE g/L, HCl, NaOH pellets, acetone, NaOCl, distilled water, 98% $CH_3COOH$, and NaCl.

### *2.2. Methods*

The isolation of chitin and chitosan from crab shells was carried out through demineralization, deproteinization, depigmentation, and deacetylation processes. The initial step was demineralization, which referred to a modified method reported by Junaidi et al. (2021). Crab shells were demineralized using a 1.5 M HCl solution at a ratio of 1:15 (w/v) at room temperature for approximately 2 hours. The demineralized product was then deproteinized using a 3.5% (w/v) NaOH solution at a ratio of 1:10 (w/v) at 65°C for 4 hours. Chitin obtained from the demineralization and deproteinization steps was depigmented using a 2% sodium

hypochlorite (NaOCl) solution at a ratio of 1:10 (w/v) at room temperature for 10 minutes.

Chitin resulting from the demineralization, deproteinization, and depigmentation steps was deacetylated using NaOH concentrations of 40% (K40%), 50% (K50%), and 60% (K60%) at a ratio of 1:15 (w/v) at 105°C for 2 hours. Solvent regeneration was performed twice. The residue was separated by decantation and washed until neutral pH was reached, after which it was dried at 80 °C to constant weight and the yield was calculated.

Chitosan characterization included the analysis of the degree of deacetylation (DD) and molecular weight (MW). The DD of chitin and chitosan was determined using Fourier transform infrared spectroscopy based on the method of Junaidi et al. (2021). Chitin and chitosan powders were prepared as pellets with KBr at a ratio of 1:100 (w/w). The pellets were analyzed for functional group absorption in the wavenumber range of 4000–400 $cm^{-1}$. The degree of deacetylation of chitin and chitosan was calculated using the Baxter equation (1).

$$DD\ (\%) = 100 - \left[\frac{A1655}{A3450} \times 155\right] \quad (1)$$

The molecular weight of chitosan was determined using the viscometry method. Chitosan solutions with concentrations of 0.025%, 0.05%, 0.075%, 0.1%, 0.15%, and 0.2% as reported by Junaidi et al. (2021) were prepared by dissolving chitosan in a mixed solvent consisting of 0.33 M acetic acid and 0.3 M NaCl. The viscosity was measured by placing 10 mL of the chitosan solution into a viscometer. The flow rate of the solution was then converted into kinematic viscosity using Equation (2).

$$\eta_{average\ kinematic} = \frac{(k_1 \times t_1)+(k_2 \times t_2)}{2} \quad (2)$$

The kinematic viscosity of the obtained solution was compared with the kinematic viscosity of the solvent, which is referred to as the relative viscosity (3):

$$\eta_{rel} = \frac{\eta_{average\ kinematic}}{\eta_{solvent}} \quad (3)$$

The relative viscosity ($\eta_{rel}$) of the chitosan solution was converted into specific viscosity ($\eta_{sp}$) to eliminate the solvent effect (4).

$$\eta_{sp} = \eta_{rel} - 1{,}0 \quad (4)$$

The effect of chitosan concentration on specific viscosity was eliminated and converted into intrinsic viscosity ($\eta$) using the Huggins equation (5):

$$\frac{\eta_{sp}}{C} = [\eta] + k'[\eta]^2 \quad (5)$$

Subsequently, the reduced viscosity ($\eta_{red}$) was determined using Equation (6):

$$\eta_{red} = \frac{\eta_{sp}}{C} \quad (6)$$

The obtained reduced viscosity ($\eta_{red}$) values were then plotted in a linear graph, resulting in the equation $y = ax + b$, where ax represents the slope = $k'[\eta]^2C$ and b represents the intercept = $[\eta]$. Based on the intrinsic viscosity value $[\eta]$, the molecular weight of chitosan was determined using the Mark–Houwink equation as shown in Equation (7).

$$[\eta] = K \times M^{\alpha} \quad (7)$$

The solubility test of chitosan in liquid smoke was conducted following the method reported by Junaidi *et al.* (2019). A mass of 0.1 g of K40%, K50%, and K60% chitosan was dissolved in 10 mL of liquid smoke at concentrations of 10%, 15%, and 20%, followed by stirring at room temperature. In addition, the solubility of chitosan in acetic acid was also evaluated by dissolving 0.1 g of K40%, K50%, and K60% chitosan in 10 mL of 1% and 2% acetic acid solutions. Solubility was qualitatively assessed using the following criteria of completely soluble, almost

completely soluble, partially soluble, slightly soluble, and insoluble.

## 3. RESULTS AND DISCUSSION

### *3.1. Chitin and Chitosan Isolation*

The demineralization process involves the removal of minerals contained in the raw material. The most dominant minerals present in crustacean shells are $CaCO_3$ and a small amount of $Ca_3(PO_4)_2$. The HCl solution reacts with these minerals to form salts and $CO_2$ gas (Aberoumand & Hoseinian, 2025). The reaction occurring in this process is as follows:

$$CaCO_{3(s)} + 2HCl_{(aq)} \rightarrow CaCl_{2(aq)} + H_2O_{(l)} + CO_{2(g)}$$

$$Ca_3(PO_4)_{2(s)} + 4HCl_{(aq)} \rightarrow 2CaCl_{2(aq)} + Ca(H_2PO_4)_{2(aq)}$$

The resulting yield was 62.65%. This value is consistent with the statement by Rochima (2014) that crab shells contain 40–60% mineral content.

The deproteinization process involves the removal of proteins present in the raw material. During this process, cleavage of protein bonds occurs, in which $Na^+$ ions derived from NaOH bind to the negatively charged ends of protein chains. The protein bonds are released to form sodium proteinate, which is soluble in water and is therefore removed during the washing of the residue. The reaction occurring in the deproteinization process is illustrated in **Figure 1.**

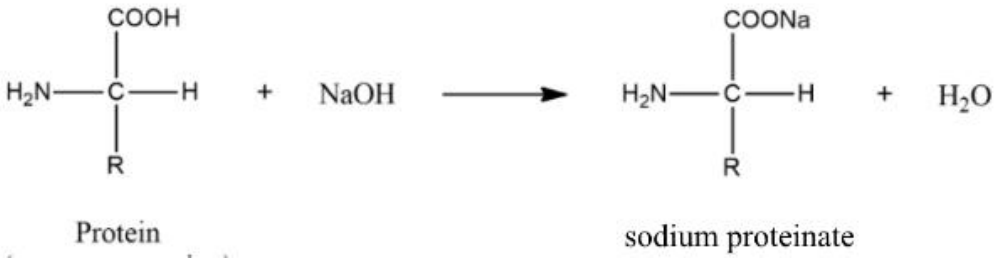


**Figure 1.** Deproteinization process

The resulting yield was 50.94%. This value differs considerably from the typical yield of the deproteinization process, in which the protein content of crustaceans generally ranges from 20–40%.

This substantial difference is likely due to the presence of residual meat and internal organs that remained attached to the outer surface of the crab shells and were removed during the deproteinization process. In addition, fine powdered residues may have been lost during the washing step and passed through during the decantation process (Korampattu, et al., 2024).

The depigmentation process involves the removal of pigments present in the raw material. In general, pigments in crab shells are dominated by astaxanthin, canthaxanthin, lutein, and β-carotene, which are carotenoid compounds (Fearghail et al., 2019; Korampattu, et al., 2024). Residual pigments present in chitin or chitosan may cause adverse effects when applied in biomedical fields. Therefore, chitin and chitosan intended for such applications must possess a high degree of purity. The yield obtained from the depigmentation process was 97.69%.

The deacetylation process involves the cleavage of acetyl groups originally present in chitin. Initially, an addition reaction occurs in which the –OH group enters the $–NH–COCH_3$ group, resulting in the elimination of the $CH_3COO^-$ group and the formation of amine groups, which are the principal functional groups of chitosan (Novikov et al., 2023).

The yields obtained for K40%, K50%, and K60% were 71.30%, 62.05%, and 56.50%, respectively. The deacetylation yield data

indicate that higher NaOH concentrations lead to lower yields.

This decrease is attributed to polymer degradation and the increased removal of acetyl groups as a result of higher alkali concentrations and elevated reaction temperatures (Fadli et al., 2017).

**Figure 1.** (a) crab shell powder, (b) residue after demineralization, (c) chitin after deproteinization, (d) chitin after depigmentation, (e) chitosan after deacetylation

Visually, the chitosan produced through the demineralization to deacetylation stages is shown in **Figure 2**. Figure 2 shows a gradual color change from image (a) to image (e). The removal of minerals from the raw material caused the residue to appear reddish brown. Chitin obtained after the deproteinization process exhibited a slightly lighter reddish color, which can be attributed to the corrosive nature of NaOH that is capable of damaging pigments in the sample. Chitin obtained after the depigmentation process appeared white, indicating that the pigments previously bound to chitin after deproteinization were effectively removed. The chitosan produced after the deacetylation process exhibited a cream or slightly yellowish color.

Chitosan is a glucose-based polymer containing reducing sugar units, in which its structure includes aldehyde groups ($CH_2OH$) and primary amine groups ($NH_2$). When chitosan is heated at temperatures above 100°C, a Maillard reaction occurs. The Maillard reaction is a non-enzymatic browning reaction between carbohydrates, particularly those containing reducing sugars, and amine groups present in the material, resulting in a brownish coloration (Ridhani et al., 2021).

### *3.2. Chitosan Characterization*

The FTIR spectra of chitin, K40%, K50%, and K60% shown in **Figure 3** indicate differences in functional groups before and after the deacetylation process. The spectral regions observed in Figure 2 include absorption peaks corresponding to O–H stretching vibrations, C–H stretching, C=O stretching, N–H bending, C–H bending, and C–O–C stretching, which are presented in **Table 1**.

The spectral regions of chitin and K40% show similar wavenumber absorptions for each observed functional group. This indicates that K40% possesses properties similar to those of chitin. The O–H stretching vibrations of K50% and K60% are observed in the absorption region at 3441 $cm^{-1}$. The absorption bands at 3109.25 $cm^{-1}$, 3263.56 $cm^{-1}$, and 3271.27 $cm^{-1}$ observed in chitin and K40% are absent in K50% and K60%,

indicating the removal of acetyl groups. The absorption band at 2885.51 $cm^{-1}$ indicates the presence of alkane C–H groups corresponding to the stretching vibration of $–CH_2–$ groups (Cakasana et al., 2014).

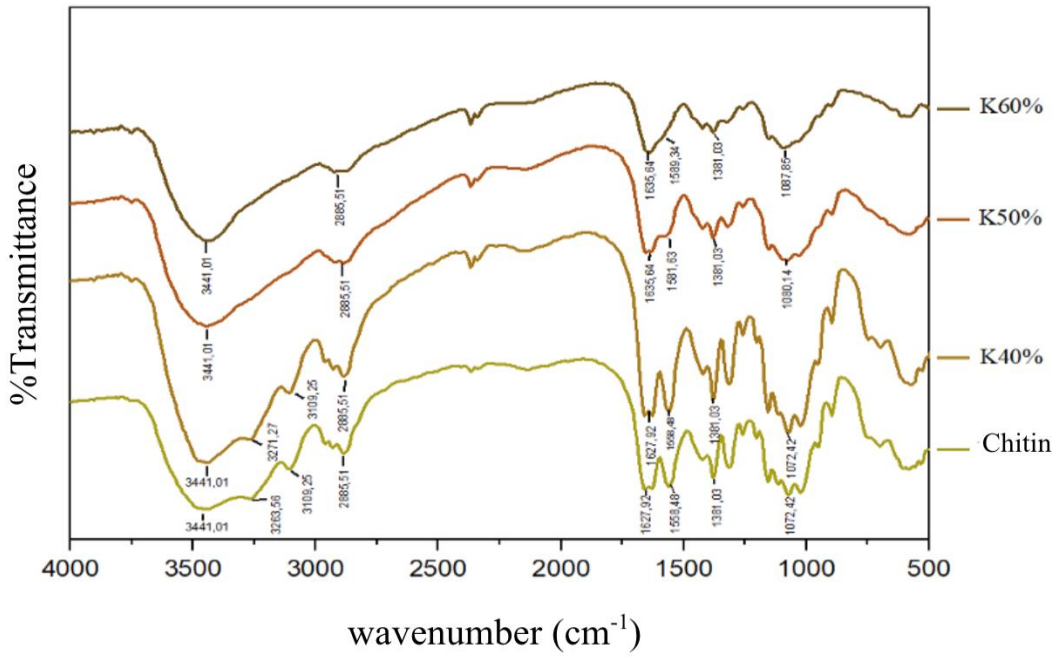


**Figure 2.** FTIR spectra of chitin and chitosan

**Table 1.** FTIR absorption functional groups of chitin and chitosan K40%, K50%, and K60%

| Functional Group | Wavenumber ($cm^{-1}$) | | | |
|---|---|---|---|---|
| | Chitin | K40% | K50% | K60% |
| O-H stretching | 3441.01 | 3441.01 | 3441.01 | 3441.01 |
| N-H stretching | 3109.25 | 3109.25 | - | - |
| C-H stretching | 2885.51 | 2885.51 | 2885.51 | 2885.51 |
| C=O stretching | 1627.92 | 1627.92 | 1635.64 | 1635.64 |
| N-H bending | 1558.48 | 1558.48 | 1581.63 | 1589.34 |
| C-H bending | 1381.03 | 1381.03 | 1381.03 | 1381.03 |
| C-O-C bending | 1072.42 | 1072.42 | 1080.14 | 1087.85 |

The peak at 1627.92 $cm^{-1}$ in chitin and K40% corresponds to the C=O stretching vibration of amide groups and shows a decrease in intensity in K50% and K60% with a shift to 1635.64 $cm^{-1}$. This indicates a reduction in secondary amide N–H groups in chitin due to the removal of acetyl groups (Azizati, 2019). The absorption band of chitin and K40% at 1558.48 $cm^{-1}$ indicates N–H bending vibrations of $R–NH_2$ and shows a decrease in intensity with shifts to 1581.63 $cm^{-1}$ for K50% and 1589.34 $cm^{-1}$ for K60%, which indicates an increase in the degree of deacetylation. According to Azizati (2019), the formation of chitosan can be identified by a decrease in the intensity of the C=O stretching and N–H bending absorption peaks that were initially sharp. The decrease in peak intensity indicates a reduction in acetyl groups in chitin. The absorption band at 1381.01 $cm^{-1}$

corresponds to C–H bending vibrations, while absorption bands at 1072.42 $cm^{-1}$, 1080.14 $cm^{-1}$, and 1080.85 $cm^{-1}$ correspond to asymmetric C–O–C stretching vibrations of the glucosamine ring (Etminanrezaeieh, et al., 2025).

The degree of deacetylation represents the percentage of acetyl group removal following the deacetylation process of chitin. The principle of DD determination using the FTIR method is based on the ratio of absorbance values of the amide group at a wavenumber of 1655 $cm^{-1}$ and the hydroxyl group at 3650 $cm^{-1}$ (Junaidi et al., 2021). According to Ghanem, et al. (2025), deacetylated chitin can be classified as chitosan when it has a degree of deacetylation of at least 70%.

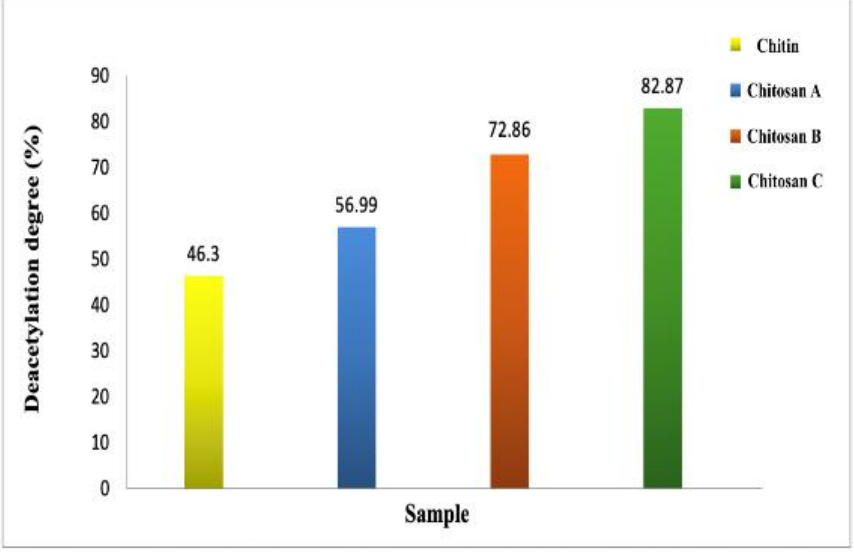


**Figure 3.** Results of DD analysis of chitin and chitosan: A (K40%), B (K50%), and C (K60%)

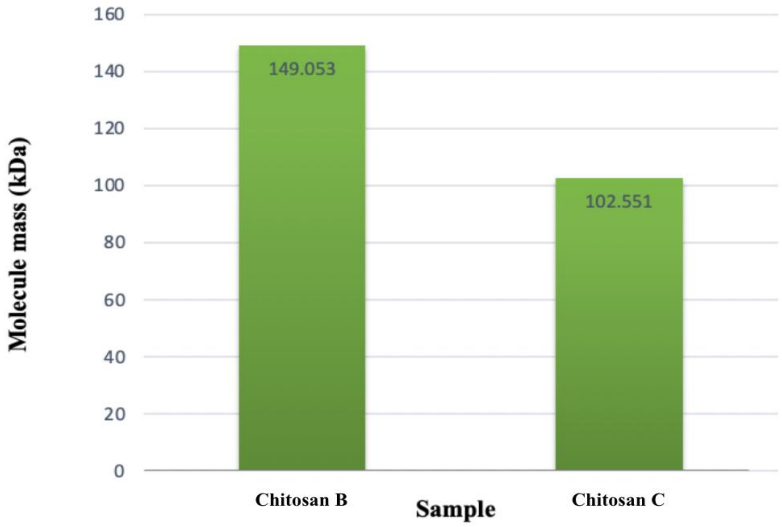


**Figure 4.** Results of molecular weight analysis of chitosan B (K50%) and chitosan C (K60%)

Based on **Figure 4**, chitin and K40% exhibit DD values of 46.4% and 56.99%, respectively, which are ≤70%. Therefore, K40% is still classified as chitin. In contrast, K50% and K60% are classified as chitosan, as they exhibit DD values of 72.84% and 82.87%, respectively. The differences in DD among K40%, K50%, and K60% are attributed to variations in the NaOH concentration used during the chitin deacetylation process.

Higher NaOH concentrations lead to a greater number of $Na^+$ and $OH^-$ ions attacking the C=O group of acetamide. This results in increased removal of acetyl groups and their substitution by amine groups, thereby increasing the DD value obtained (Amitaye, et al., 2024).

The NaOH concentration used in the deacetylation process also affects the molecular weight of the resulting chitosan. The molecular weight determination of K50% and K60% was carried out using the viscometry method. The results are presented in **Figure 5**.The molecular weight analysis of chitosan K40%, K50%, and K60% were performed using the viscometry method. However, K40% chitosan did not dissolve in the solvent used, and therefore its molecular weight analysis was not carried out. Based on Figure 5, chitosan K50% exhibited a molecular weight of 149.1 kDa, while K60% exhibited a molecular weight of 102.6 kDa. According to Román-Doval, et al. (2023), chitosan with a molecular weight in the range of 50–150 kDa is classified as having medium molecular weight. The molecular weight of K50% was higher than that of K60% due to differences in the NaOH concentration used during the deacetylation process.

Higher NaOH concentrations result in lower molecular weight. This effect occurs because acetyl groups are removed and replaced by amine groups, which influences the molecular weight of chitosan and leads to a decrease as more acetyl groups are removed. In addition, the use of high NaOH concentrations during deacetylation can cause depolymerization. Increasing NaOH concentration leads to shorter polymer chains as a result of cleavage of glycosidic bonds between chitosan molecules, thereby reducing the molecular weight of the chitosan produced (Periyannan et al., 2023).

### *3.3. Chitosan Solubility*

One of the important parameters influencing the application of chitosan is its solubility. Chitosan solubility was evaluated in acetic acid and in liquid smoke. The observed solubility results of chitosan in these two media are presented in **Table 2**.

Based on **Table 2**, K40% was insoluble in both acetic acid and liquid smoke. This result is attributed to the DD value of K40%, which was 56.99% or less than 70%, indicating that it is still classified as chitin. Chitosan K50% was completely soluble in 2% acetic acid and 20% liquid smoke, while it was partially soluble in 1% acetic acid and almost completely soluble in 10% and 15% liquid smoke. Chitosan K60% exhibited good solubility in acetic acid at concentrations of 1–2% and in liquid smoke at concentrations of 10–20%. These results are consistent with the findings reported by Junaidi et al. (2019) who stated that liquid smoke at concentrations of at least 5% is capable of dissolving more than 50 g/L of chitosan.

Based on the solubility behavior of K40%, K50%, and K60%, it can be concluded that higher degrees of deacetylation lead to increased chitosan solubility. This is because a higher DD corresponds to a greater abundance of amine groups, which play a key role in the dissolution process. In addition, chitosan solubility is directly proportional to the concentration of liquid smoke used, where

higher liquid smoke concentrations result in greater chitosan solubility. This effect occurs because higher concentrations of liquid smoke contain higher total acid content, which increases the protonation of chitosan amine groups to $NH_3^+$ due to the abundance of $H_3O^+$ ions present in the liquid smoke (Junaidi et al., 2019). Following protonation of the amine groups, electrostatic repulsion between $NH_3^+$ groups occur. This repulsion disrupts attractive interactions between polymer chains such as hydrogen bonding and hydrophobic interactions, leading to the dissolution of chitosan (Saïed & Aider, 2014).

**Tabel 2.** Solubility test results of chitosan in liquid smoke

| Solvent | Solvent Concentration | Solvent pH | K40% | K50% | K60% |
|---|---|---|---|---|---|
| Acetic acid | 1% | 2.8 | Insoluble | Partially soluble | Completely soluble |
| | 2% | 2.6 | Slightly soluble | Completely soluble | Completely soluble |
| Coconut shell liquid smoke | 10% | 3.2 | Insoluble | Almost completely soluble | Completely soluble |
| | 15% | 3.1 | Insoluble | Almost completely soluble | Completely soluble |
| | 20% | 3.1 | Slightly soluble | Completely soluble | Completely soluble |

## 4. CONCLUSIONS

Based on the results of this study, it can be concluded that the NaOH concentration used in the chitin deacetylation process significantly affects the degree of deacetylation and molecular weight of the resulting chitosan. Higher NaOH concentrations produce chitosan with higher degrees of deacetylation and lower molecular weights. Chitosan with a high degree of deacetylation and low molecular weight exhibits greater solubility in liquid smoke. In 10% liquid smoke, K40% was insoluble, K50% was almost completely soluble, and K60% was completely soluble. The results of this study provide scientific support for the potential application of a combination of chitosan and liquid smoke without requiring additional solvents.

## ACKNOWLEDGMENT

The authors would like to express their sincere gratitude to the Institute for Research and Community Service (LPPM), Universitas Lambung Mangkurat, for the financial support and facilities provided to carry out this research. The authors also acknowledge technical assistance and support from all parties who contributed directly or indirectly to the completion of this study.

## LIST OF REFERENCES

Aberoumand, A., & Hoseinian, M. (2025). Extraction and characterization of chitosan obtained from shells of crab (*Liocarcinus vernalis*). *Applied Food Research, 5*(1), 100964. https://doi.org/10.1016/j.afres.2025.100964

Amitaye, A. N., Elemike, E. E., & Uzah, T. T. (2024). Multifarious techniques for resolving chitosan's degree of deacetylation. *Materials International, 6*(2), 1–24.https://https/doi.org/10.33263/Materials62.016

Azizati, Z. (2019). Pembuatan dan karakterisasi kitosan kulit udang galah. *Walisongo Journal of Chemistry, 2*, 10–16. https://doi.org/10.21580/wjc.v3i1.3878

Cakasana, N., Suprijanto, J., & A. S. (2014). Aktivitas antioksidan kitosan yang diproduksi dari cangkang kerang simpling (*Amusium* sp.) dan kerang darah (*Anadara* sp.). *Journal of Marine Research, 3*, 395–404. https://doi.org/10.14710/jmr.v3i4.8360

Etminanrezaeieh, S., Rezazadeh, K., Jalilnejad, E., & Reza, R. (2025). Preparation and characterization of bio-waste derived chitosan hydroxyapatite pectin green biocomposite. *Scientific Reports, 15*, 24450. https://doi.org/10.1038/s41598-025-07588-0

Fadli, A., Drastinawati, O., Alexander, O., & F. H. (2017). Effect of chitin mass NaOH ratio and reaction time on characteristics of chitosan synthesized from waste of dried shrimp industry. *Jurnal Sains Materi Indonesia, 18*, 61–67. https://doi.org/10.17146/jsmi.2017.18.2.4166

Fearghail, F. O., Giltrap, M., O'Connor, C. O., & P. B. (2019). Improving extraction processes of crustacean chitin using solid state analytical techniques. *International Journal of Applied Chemistry, 6*, 23–30.

Ghanem, S. N., Marzouk, M. I., Tawfik, M. E., & Eskander, S. B. (2025). Spectroscopic approaches for structural analysis of extracted chitosan generated from chitin deacetylated for escalated periods. *BMC Chemistry, 19*, 214. https://doi.org/10.1186/s13065-025-01558-3

Junaidi, A. B., Apriyani, H., Abdullah, A., & Santoso, U. T. (2019). Fraksinasi dan karakterisasi asap cair dari kayu ulin (*Eusideroxylon zwageri* Teijsm. & Binn.) sebagai pelarut kitosan. *Jurnal Riset Industri Hasil Hutan, 11*, 53–64.

Junaidi, A. B., Irawati, U., & Santoso, U. T. (2021). *Teknologi kitin dan kitosan: Definisi, preparasi dan karakterisasi*. Banyubening Cipta Sejahtera.

Korampattu, L., Neha, G., & Paresh, L. D. (2024). Shell waste valorization to chemicals: Methods and progress. *Green Chemistry, 26*, 5601–5634. https://doi.org/10.1039/D3GC05177C

Niu, Y., & Hu, W. (2024). Preparation, characterization and application in environmental protection of low-molecular-weight chitosan: A review. *Sustainable Environment Research, 34*, 29. https://doi.org/10.1186/s42834-024-00236-8

Nurhikmawati, F., Manurung, M., & Laksmiwati, A. A. I. A. M. (2014). Penggunaan kitosan dari limbah kulit udang sebagai inhibitor keasaman tuak. *Jurnal Kimia, 8*, 191–197. https://doi.org/10.24843/JCHEM.2014.v08.i02.p08

Novikov, V. Y., Derkach, S. R., Konovalova, I. N., Dolgopyatova, N. V., & Kuchina, Y. A. (2023). Mechanism of heterogeneous alkaline deacetylation of chitin: A review. *Polymers, 15*(7), 1729. https://doi.org/10.3390/polym15071729

Periyannan, K., Selvaraj, H., Subbu, B., Pallikondaperumal, M., Karuppiah, P., Rajabathar, J., Al-Lohedan, H., & Thangarasu, S. (2023). Green fabrication of chitosan from marine crustaceans and mushroom waste: Toward sustainable resource utilization. *Green Processing and Synthesis, 12*(1), 20230093. https://doi.org/10.1515/gps-2023-0093

Ridhani, M. A., Vidyaningrum, I. P., Akmala, N. N., Fatihatunisa, R., Azzahro, S., & Aini, N. (2021). Potensi penambahan berbagai jenis gula terhadap sifat sensori dan fisikokimia roti manis: A review. *Pasundan Food Technology Journal, 8*, 61–68. https://doi.org/10.23969/pftj.v8i3.4106

Rochima, E. (2014). Study of utilization of crabs processing wastes and its application for chitosan-based healthy drink. *Akuatika, 5*(1), 71–82. https://jurnal.unpad.ac.id/akuatika/article/view/3707

Román-Doval, R., Torres-Arellanes, S. P., Tenorio-Barajas, A. Y., Gómez-Sánchez, A., & Valencia-Lazcano, A. A. (2023). Chitosan: Properties and its application in agriculture in context of molecular weight. *Polymers, 15*(13), 2867. https://doi.org/10.3390/polym15132867

Saïed, N., & Aïder, M. (2014). Zeta potential and turbidimetry analyses for the evaluation of chitosan phytic acid complex formation. *Journal of Food Research, 3*(2), 71–81. https://doi.org/10.5539/jfr.v3n2p71

Saravanan, A., Kumar, P., Yuvaraj, D., Jeevanantham, S., Aishwaria, P., Gnanasri, P. B., Gopinath, M., & Rangasamy, G. (2023). Polysaccharides from crustacean wastes and their environmental applications. *Environmental Research, 221*, 115330. https://doi.org/10.1016/j.envres.2023.115330

Vo, T. S., Chit, P. P., Hoang, T., Hoang, V. H., Dang, T. T., Vo, T. T. B. C., Park, Y., & Kim, K. (2025). Chitosan solubility in organic acid solutions under ultrasonication: A comparative perspective. *International Journal of Biological Macromolecules, 331*(Pt 1), 148394. https://doi.org/10.1016/j.ijbiomac.2025.148394

Wang, H., & Roman, M. (2023). Effects of chitosan molecular weight and degree of deacetylation on chitosan cellulose nanocrystal complexes and their formation. *Molecules, 28*(3), 1361. https://doi.org/10.3390/molecules28031361

Zuwanna, I., Riza, M., Aprilia, S., Syamsuddin, Y., Said, S., & Dewi, R. (2025). Investigation of characteristics whey protein isolate chitosan with silica addition in biocomposite film. *International Journal of Technology, 16*(1), 359–369. https://doi.org/10.14716/ijtech.v16i1.6335

**Jurnal Ilmiah Berkala: Sains dan Terapan Kimia**
*Vol. 20 No. 1, January 2026*

# Network Pharmacology-Based Evaluation of Sungkai (*Peronema canescens* J.) Leaf Bioactive Compounds as Potential Therapeutics for Cervical Cancer

# Evaluasi Berbasis *Network Pharmacology* Senyawa Bioaktif Daun Sungkai (Peronema canescens J.) sebagai Kandidat Terapi Kanker Serviks

**Ratih Dyah Puspitasari[1*], Ahmad Sazali[2], and Indra Lasmana Tarigan[1]**

[1]Department of Chemistry, Faculty of Science and Technology, Universitas Jambi, Jambi, Indonesia, 36361
[2]Department of Biology, Faculty of Science and Technology, Universitas Jambi, Jambi, Indonesia, 36361

Email: ratihdyah@unja.ac.id

**ABSTRACT**

*Cervical cancer continues to pose a significant public health challenge, especially in low- and middle-income countries, largely due to persistent Human Papillomavirus (HPV) infection and the limited efficacy and safety of current therapies. Although flavonoid-based anticancer agents such as jaceosidin have shown anticancer activity, their clinical use is limited by low bioavailability and insufficient clinical evidence, underscoring the need for safer, more effective therapeutic options. This study utilized in silico and network pharmacology methods to assess bioactive compounds from Sungkai leaves (Peronema canescens* J.*). Seven peronemin derivatives were evaluated for drug-likeness, toxicity, and anticancer potential through ADMET predictions, bioactivity profiling, and protein target identification. The findings demonstrated that peronemin C1 and D1 possess activity against cervical cancer cell lines and exhibit favorable pharmacokinetic properties. Network pharmacology analysis identified 115 cancer-associated targets, with STAT3 identified as a central hub regulating cell proliferation, apoptosis, and inflammatory signaling. Functional analyses further indicated that peronemin compounds modulate key oncogenic pathways, supporting their multitarget potential. Collectively, these results indicate that peronemin compounds from Sungkai leaves, particularly C1 and D1, are promising candidates for the development of cervical cancer therapies targeting STAT3.*

**Keywords**: Cervical cancer; peronemin; STAT3; network pharmacology..

**Received**: 23 December 2025; **Accepted**: 23 January 2026: **Available online**: 29 January 2026

## 1. INTRODUCTION

Cancer remains a leading cause of mortality worldwide. It poses a significant public health challenge. According to the World Health Organization (WHO, 2020), cancers of the breast, lung, colon, cervix, liver, and skin account for a substantial proportion of global cancer-related deaths. Cervical cancer disproportionately affects low- and middle-income countries (LMICs), accounting for 84–90% of global cases and deaths. This elevated burden results primarily from

disparities in screening, human papillomavirus (HPV) vaccination, and access to treatment. Sub-Saharan Africa, South and Southeast Asia, and Latin America are particularly affected, as limited preventive services contribute to persistently high incidence and mortality rates (Hull et al., 2020). This is largely due to persistent human papillomavirus (HPV) infection and limited access to early detection and treatment strategies. Medical treatments, such as surgery, radiotherapy, and chemotherapy, have advanced significantly. Drug resistance, severe side effects, and incomplete tumor eradication often hinder patient outcomes. Both intrinsic and acquired mechanisms allow cancer cells to survive treatment by adapting through genetic and epigenetic alterations. These changes lower drug sensitivity, leading to relapse, treatment failure, and disease progression (Nikolaou et al., 2018). There is an urgent need to discover novel therapeutic compounds with improved efficacy and safety profiles.

Plant-derived bioactive compounds have emerged as a promising source for the development of anticancer drugs. Numerous studies have explored the potential of phytochemicals in modulating cancer-related pathways, both in vitro and in vivo. These natural compounds often exhibit multitarget activity, low toxicity, and synergistic effects with conventional drugs. For example, jaceosidin shows potential anticancer activity through several mechanisms: it induces apoptosis, inhibits cell proliferation, and modulates signaling pathways linked to cancer cell growth in many cancer cell lines. In cervical cancer, jaceosidin inhibits the HPV-16 E6 and E7 oncoproteins, restores p53 and Rb activity, and suppresses the survival of cervical cancer cell lines such as SiHa and CaSki (Lee et al., 2019). Although jaceosidin shows promising pharmacological activity, several challenges limit its potential as an anticancer agent. The primary limitations include low bioavailability and limited metabolic stability. Jaceosidin exhibits poor absorption and low systemic availability. Additionally, it undergoes rapid metabolism into conjugates, which further diminishes its effective concentration at target sites (Nageen et al., 2021).

Advances in computational approaches have significantly helped the discovery of anticancer drugs. In silico methods enable the identification of candidate drug targets by analyzing compound–protein interactions. These methods support the design, optimization, and screening of new bioactive molecules (Malikhana et al., 2021). Network pharmacology systematically integrates biological and pharmacological data to reveal how bioactive compounds interact with molecular targets and disease pathways. This approach is especially valuable for studying natural products with multi-target effects, as it uncovers synergistic interactions between chemical constituents and cancer-related genes, proteins, and metabolic pathways. By mapping compound–target–pathway relationships, network pharmacology provides a clear framework for understanding the molecular basis of anticancer activity (Poornima et al., 2016; Lee et al., 2019; Zhang et al., 2020).

Sungkai (Peronema canescens) is a medicinal plant with promising anticancer properties. Its leaf extracts contain bioactive compounds such as β-sitosterol, phytol, β-amyrin, and several peronemin derivatives (A1, A3, B1–B3, C1) (Ibrahim & Kuncoro, 2012; Kitagawa et al., 1994). Previous studies reported that Sungkai extracts inhibit the

growth of colon cancer cells and affect the proliferation of HeLa cells (Ibrahim et al., 2021). Nevertheless, the multitarget anticancer mechanisms of Sungkai-derived bioactive compounds remain largely uncharacterized.

In this study, network pharmacology and computer-based multitarget analysis were used to systematically study the anticancer potential of active compounds from Sungkai (*Peronema canescens* J.) leaves. This method helps find disease-related targets, compound–target links, and main biological pathways in cervical cancer. Using a systems approach, the study aims to explain how Sungkai bioactives work in cervical cancer and to support the identification of new plant-based anticancer candidates with multitarget effects.

## 2. MATERIALS AND METHODS

### *2.1. Materials*

The bioactive compounds analyzed in this study were derived from Sungkai (*Peronema canescens*) leaves. Seven peronemin derivatives (Peronemin A2, A3, B1, B2, B3, C1, and D1) were selected based on previous phytochemical studies. The two-dimensional (2D) chemical structures of these compounds were obtained from the literature (Kitagawa et al., 1994). They were then converted into three-dimensional (3D) structures and SMILES representations using ChemSketch version 2015 (ACD/Labs, Canada). In this study Jaceosidin was used as a reference compound to compare predicted pharmacokinetic properties and multitarget interactions.

### *2.2. Methods*

#### *2.2.1 Data mining of Bioactive Compounds*

The 2D structures of seven bioactive compounds were converted into 3D structures and SMILES representations. This was based on the study by Kitagawa et al. (1994). The construction of the 3D structures and SMILES was carried out using ChemSketch v.2015 software.

#### *2.2.2 ADMET Analysis*

Drug-likeness characteristics were determined for each compound according to Lipinski's Rule of Five. Analysis was conducted using the ProTox II database (https://tox-new.charite.de/protox_II/index.php?site=compound_input) (Drwal et al., 2014; Banerjee et al., 2018) and the ADMETLab 2.0 database (https://admetmesh.scbdd.com/service/evaluation/index ) (Dong et al., 2018; Xiong et al., 2021). The SMILES representation of each ligand was entered into both databases.

#### *2.2.3 Bioactivity Prediction*

The Sungkai compounds were subsequently analyzed using CLC-Pred 2.0 (https://www.way2drug.com/clc-pred/) (Lagunin et al., 2018) to evaluate their potential bioactivity potential and relevant cancer cell lines for cervical cancer.

#### *2.2.4 Protein Target Prediction*

Target proteins were analyzed using the SEA Search Server (https://sea.bkslab.org/) (Keiser et al., 2007), SwissTargetPrediction (http://www.swisstargetprediction.ch/) (Daina et al., 2019), TargetNet (http://targetnet.scbdd.com/calcnet/index/) (Yao et al., 2016), BindingDB (https://www.bindingdb.org/rwd/bind/index.jsp) (Gilson et al., 2015), PASS Targets (https://www.way2drug.com/passtargets/) (Pogodin et al., 2015), and SuperPred (https://prediction.charite.de/subpages/target_prediction.php) (Nickel et al., 2014).

#### *2.2.5 Data mining Gene-Diseases Associations Cervical Cancer*

The list of proteins and genes associated with cervical cancer was obtained from the DisGeNET database(https://www.disgenet.org/search) (Piñero et al., 2020), Open Targets

(https://www.opentargets.org/), GeneCards (https://www.genecards.org/) (Stelzer et al., 2016), OMIM(https://www.omim.org/), and UniProt (https://www.uniprot.org/) (Coudert et al., 2023).

*2.2.6 Network Pharmacology Analysis*

The intersection between the predicted targets of sungkai bioactive compounds and disease-associated genes was subsequently subjected to protein–protein interaction (PPI) analysis using the STRING DB V.12 with the following parameters: organism set to *Homo sapiens*, network type as full STRING network, interaction score set to high confidence, and STRING false discovery rate (FDR) stringency set to medium (5%). The STRING output in TSV format was further processed using Cytoscape v10. Cytoscape was used to visualize the interaction data and to perform network analysis. Several Cytoscape plugins were employed to identify the most influential target proteins within the network. The MCODE plugin was used to cluster specific networks based on topology to identify densely connected regions. Proteins within the densest clusters were considered highly connected to other proteins in the network; therefore, targeting these proteins may influence multiple interacting proteins. The CytoHubba plugin (Chin et al., 2014) was used to predict hub proteins in the network. Hub proteins are defined as proteins that interact with many other proteins. The Maximal Clique Centrality (MCC) algorithm implemented in CytoHubba was applied to identify the top 10 hub proteins in the network. In addition, centrality analysis was performed to determine the proteins with the most critical roles in the interaction between *Sungkai* bioactive compounds and cervical cancer. The centrality measures used were Degree Centrality (DC), Betweenness Centrality (BC), and Closeness Centrality (CC).

*2.2.7 Functional Analysis*

The Database for Annotation, Visualization, and Integrated Discovery (DAVID) (Sherman et al., 2021) was used to identify the functions of genes from the Venn diagram intersection. We further discussed terminologies with a false discovery rate (FDR) < 0.05. Annotations were based on Gene Ontology and the Kyoto Encyclopedia of Genes and Genomes (KEGG).

## 3. RESULTS AND DISCUSSION

*3.1. Data Mining Bioactive Compound of Sungkai Leaf*

The chemical structures of peronemin compounds were obtained through data mining from previously published phytochemical studies, particularly from Kitagawa et al. (1994), which reported the isolation and structural elucidation of peronemin derivatives from Peronema canescens. These structures were subsequently used for further computational analyses, including target prediction and network pharmacology evaluation (**Figure 1**).

*3.2. ADMET Analysis*

ADMET properties—absorption, distribution, metabolism, excretion, and toxicity are important in drug discovery. The ADMETlab 2.0 database (**Table 1**) was used to predict Lipinski's rule and ADME/T properties for the compounds. The ProTox II database (Drwal et al., 2014) was also used to verify compliance with Lipinski's rule and assess toxicity (**Table 2**). Lipinski's Rule of Five helps identify drug-like molecules by comparing them to known pharmacologically active compounds. Compounds that meet at least two of the five main criteria are

considered to satisfy Lipinski's rule (Lipinski et al., 1997).

The Lipinski Rule of Five includes the following criteria: molecular weight less than 500 Da, high lipophilicity (expressed as LogP < 5), fewer than five hydrogen bond donors, fewer than ten hydrogen bond acceptors, and molecular refractivity between 30 and 140.

Nevertheless, drug-likeness does not indicate that the remaining compounds lack therapeutic potential; rather, they may require higher energy input or active transport mechanisms to be localized within cells. Meanwhile, ADMET analysis (absorption, distribution, metabolism, excretion, and toxicity) showed that nearly all compounds exhibited favorable pharmacodynamic and pharmacokinetic properties.

Absorption analysis revealed that all compounds exhibited favorable Human Intestinal Absorption (HIA) values, with predicted probabilities below 0.30, consistent with good intestinal absorption according to ADMETLab 2.0 criteria, compounds with HIA values < 30% are classified as having good intestinal absorption (Xiong et al., 2021). These results suggest that the peronemin derivatives possess physicochemical properties conducive to oral administration. Notably, Peronemin D1 showed a high probability of achieving oral bioavailability greater than 20%, while Peronemin A2, B2, and C1 demonstrated favorable probabilities at the 30% threshold, indicating their potential to reach therapeutically relevant plasma concentrations following oral dosing.

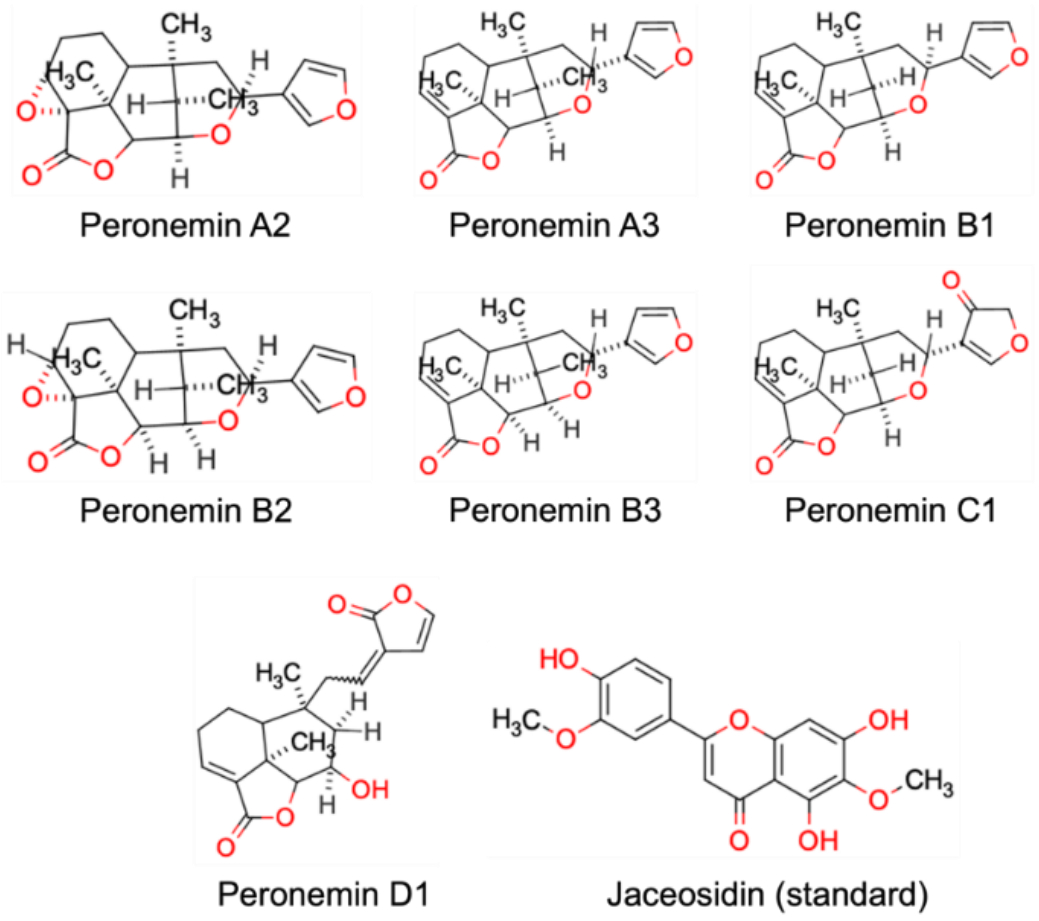


**Figure 1**. Chemical structure of peronemin compounds

**Table 1**. Drug-likeness and ADMET profiling of potential compounds predicted by ADMETLab 2.0

| No | Compounds | Lipinski | HIA | F(20%) | F(30%) | BBB | DILI | Carcinogenicity |
|---|---|---|---|---|---|---|---|---|
| 1 | Peronemin A2 | Accepted | 0.004 | 0.104 | 0.858 | 0.307 | 0.521 | 0.738 |
| 2 | Peronemin A3 | Accepted | 0.012 | 0.145 | 0.05 | 0.596 | 0.357 | 0.051 |
| 3 | Peronemin B1 | Accepted | 0.006 | 0.067 | 0.255 | 0.291 | 0.19 | 0.036 |
| 4 | Peronemin B2 | Accepted | 0.003 | 0.027 | 0.535 | 0.203 | 0.367 | 0.512 |
| 5 | Peronemin B3 | Accepted | 0.01 | 0.028 | 0.044 | 0.301 | 0.282 | 0.023 |
| 6 | Peronemin C1 | Accepted | 0.007 | 0.009 | 0.592 | 0.33 | 0.224 | 0.027 |
| 7 | Peronemin D1 | Accepted | 0.043 | 0.934 | 0.157 | 0.088 | 0.062 | 0.07 |

Notes: HIA= Human Intestinal Absorption; F(20%), F(30%): oral bioavailibility; BBB= blood brain-barrier; DILI= drug-induced liver injury

**Table 2**. Toxicity Analysis of potential compounds Predicted by ProTox II

| No | Compounds | Hepatotoxicity | Carcinogenicity | Immunotoxicity | Mutagenicity | Cytotoxicity |
|---|---|---|---|---|---|---|
| 1 | Peronemin A2 | Inactive | Inactive | Active | Inactive | Inactive |
| 2 | Peronemin A3 | Inactive | Active | Active | Inactive | Inactive |
| 3 | Peronemin B1 | Inactive | Active | Active | Inactive | Inactive |
| 4 | Peronemin B2 | Inactive | Inactive | Active | Inactive | Inactive |
| 5 | Peronemin B3 | Inactive | Active | Active | Inactive | Inactive |
| 6 | Peronemin C1 | Inactive | Active | Active | Inactive | Inactive |
| 7 | Peronemin D1 | Inactive | Active | Active | Inactive | Inactive |

**Table 3.** CLC-Pred–based prediction of antiproliferative activity of bioactive compounds against cancer cell lines

| Compounds | Cell-line | Description | Tissue/ Organ | Type | IAP* |
|---|---|---|---|---|---|
| Jaceosidin | HeLa | Cervical adenocarcinoma | Cervix | Adenocarcinoma | 0.885 |
| Jaceosidin | MDA-MB-231 | Breast adenocarcinoma | Breast | Adenocarcinoma | 0.881 |
| Jaceosidin | SW1990 | Pancreatic adenocarcinoma | Pancreas | Adenocarcinoma | 0.876 |
| Jaceosidin | SW48 | Colorectal Adenocarcinoma | Colon | Adenocarcinoma | 0.806 |
| Jaceosidin | AGS | Gastric adenocarcinoma | Stomach | Adenocarcinoma | 0.875 |
| Peronemin A2 | MDA-MB-231 | Breast adenocarcinoma | Breast | Adenocarcinoma | 0.881 |
| Peronemin A2 | SW480 | Colon adenocarcinoma | Colon | Adenocarcinoma | 0.932 |
| Peronemin A2 | SW1116 | Colorectal Adenocarcinoma | Colon | Adenocarcinoma | 0.864 |
| Peronemin A3 | OVCAR-5 | Ovarian adenocarcinoma | Ovarium | Adenocarcinoma | 0.866 |
| Peronemin A3 | SW1990 | Pancreatic adenocarcinoma | Pancreas | Adenocarcinoma | 0.876 |
| Peronemin B1 | OVCAR-5 | Ovarian adenocarcinoma | Ovarium | Adenocarcinoma | 0.866 |

| Compounds | Cell-line | Description | Tissue/ Organ | Type | IAP* |
|---|---|---|---|---|---|
| Peronemin B1 | SW1990 | Pancreatic adenocarcinoma | Pancreas | Adenocarcinoma | 0.876 |
| Peronemin B2 | MDA-MB-231 | Breast adenocarcinoma | Breast | Adenocarcinoma | 0.881 |
| Peronemin B2 | SW480 | Colon adenocarcinoma | Colon | Adenocarcinoma | 0.932 |
| Peronemin B2 | SW1116 | Colorectal Adenocarcinoma | Colon | Adenocarcinoma | 0.864 |
| Peronemin B3 | OVCAR-5 | Ovarian adenocarcinoma | Ovarium | Adenocarcinoma | 0.866 |
| Peronemin B3 | SW1990 | Pancreatic adenocarcinoma | Pancreas | Adenocarcinoma | 0.876 |
| Peronemin C1 | OVCAR-5 | Ovarian adenocarcinoma | Ovarium | Adenocarcinoma | 0.866 |
| Peronemin C1 | HT-29 | Colon adenocarcinoma | Colon | Adenocarcinoma | 0.888 |
| Peronemin C1 | SW1116 | Colorectal Adenocarcinoma | Colon | Adenocarcinoma | 0.864 |
| Peronemin C1 | Bel7402/5-FU | Human papillomavirus-related endocervical adenocarcinoma | Uterus; Cervix | Adenocarcinoma | 0.966 |
| Peronemin D1 | HT-29 | Colon adenocarcinoma | Colon | Adenocarcinoma | 0.888 |
| Peronemin D1 | MKN-74 | Gastric tubular adenocarcinoma | Stomach | Adenocarcinoma | 0.856 |
| Peronemin D1 | Bel7402/5-FU | Human papillomavirus-related endocervical adenocarcinoma | Uterus; Cervix | Adenocarcinoma | 0.966 |

Notes : *IAP = Invariant Accuracy of Prediction

### *3.3. Bioactivity Prediction*

Cervical cancer is a common adenocarcinoma that often resists standard chemotherapy. In this study, Jaceosidin served as a comparison compound because it has proven anticancer effects on several cancer cell types, including HeLa cervical cells (**Table 3**).

This study is the first comprehensive investigation of peronemin derivatives from *Peronema canescens* in cervical cancer using an integrated *in silico* and network pharmacology approach. Jaceosidin, a well-characterized plant anticancer flavonoid, was included as a reference for evaluating the pharmacological relevance of peronemin derivatives. This comparison highlights peronemin as a previously underexplored multitarget scaffold, offering novel mechanistic insight and supporting its candidacy for anticancer drug development.

### *3.4. Data mining of cervical cancer and Peronemin*

Target protein prediction analysis based on six databases demonstrated that 97 targets were shared between Peronemin and the reference compound jaceosidin (**Figure 2**). In addition, jaceosidin was predicted to interact with a greater number of proteins (312) than Peronemin (231), which may be attributed to differences in structural features and target-binding diversity. Nevertheless, the substantial overlap suggests that Peronemin may exhibit biological activities comparable to those of jaceosidin.

Comparative analysis with cervical cancer–associated proteins obtained from five databases revealed that 64 of the 4,936 disease-related targets overlapped with Peronemin, while 51 targets were commonly shared among Peronemin, jaceosidin, and cervical cancer (**Figure 2b**; **Table 4**). These

common targets are likely to represent critical molecular nodes involved in cervical cancer–related signaling networks. Given the complex and multifactorial nature of cervical cancer, the ability of Peronemin to interact with multiple disease-associated targets supports its potential role in modulating key biological processes and pathways implicated in cancer progression. This multitarget interaction profile is consistent with the principles of network pharmacology and provides a rationale for subsequent pathway enrichment and experimental validation studies to elucidate the underlying molecular mechanisms.

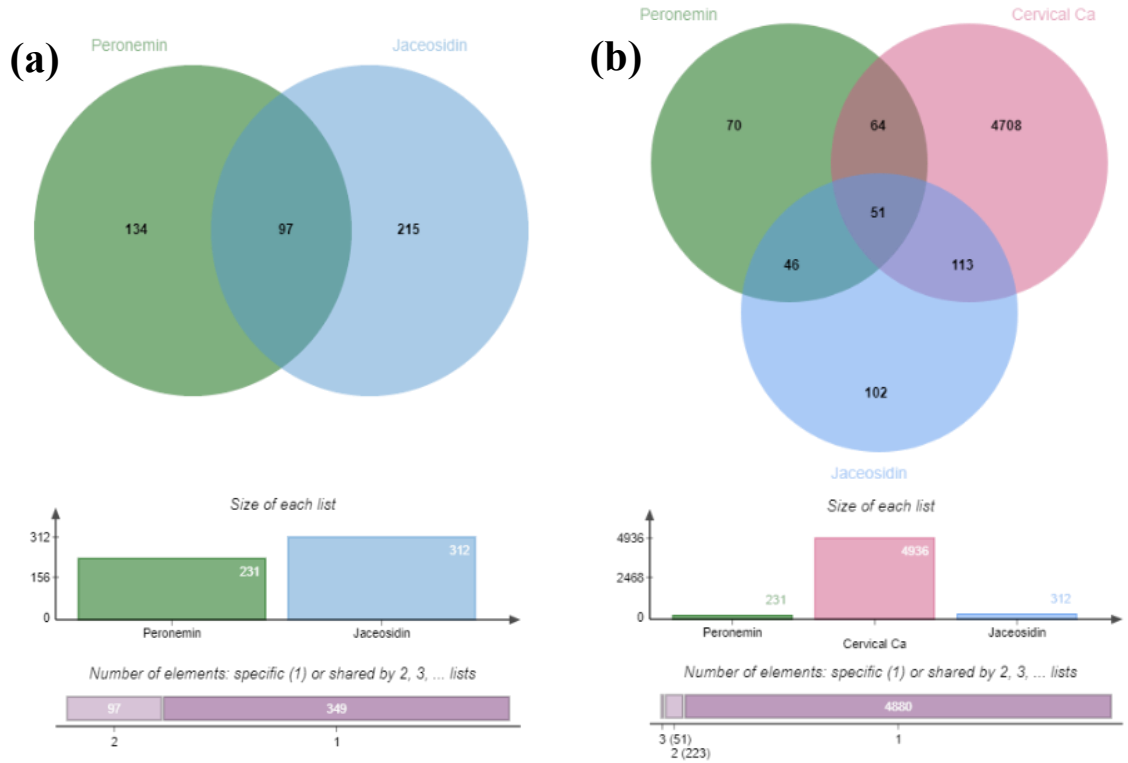


**Figure 2**. (a) Prediction of Peronemin and Jaceosidine Target Proteins; (b) Cross-target analysis of proteins targeted by Peronemin with cervical cancer–associated proteins, including control compounds (Jaceosidin)

**Table 4**. Details of proteins shared across targets

| Group | Genes |
|---|---|
| Peronemin dan Cervical Cancer | ABL1, ACACA, APOBEC3A, BCL6, BLM, BRD2, BRD3, BRD4, CARM1, CDK2, CDK4, CHUK, CNR1, CNR2, CTSB, CTSF, CTSK, CTSL, CTSS, CYP2A6, CYSLTR2, DPP4, DUT, FFAR2, GHSR, GRK5, GSK3A, HDAC1, HDAC10, HDAC2, HDAC4, HDAC6, HDAC9, HPGD, ITGB1, ITK, KDM4A, KIF11, LNPEP, MAP2K2, MAPK1, MMP1, MTOR, NOS3, P2RX7, PDGFRA, PDGFRB, PIK3CB, PKN2, PRKCD, PRKCE, |

| Group | Genes |
|---|---|
| | PRMT5, PRSS1, PSMB2, PSMB9, PTK2B, PTPN2, SAE1, STAT3, STING1, TGM2, TLR4, TLR8, WDR5 |
| Peronemin, Jaceosidin, dan Cervical Cancer | ABCB1, ADAM10, ALOX12, APEX1, AR, AURKB, CAPN1, CCNE1, CDC25C, CDK1, CDK5, CFTR, CSNK2B, CTSD, DPP9, DUSP3, DYRK1A, EGFR, F13A1, HDAC8, HIF1A, HSD17B10, HSP90AA1, HSP90AB1, KDM1A, KDR, KEAP1, KLF5, LDHB, MME, NFE2L2, NFKB1, NOS2, NR0B1, NR3C2, NTRK3, PIK3R1, PIN1, PKN1, PRKAA1, PTGS1, PTGS2, PTPN11, RPS6KA1, SERPINE1, SLC2A1, SLC9A1, TLR9, TNKS2, TOP2A, TRIM24 |

*3.5. Network Analysis*

Of the 115 proteins shared between Peronemin and cervical cancer, STAT3, EGFR, HSP90AA1, and HSP90AB1 exhibited the highest degree centrality (DC) values within the protein–protein interaction (PPI) network. This results indicates their central roles as network hubs in the Peronemin–cervical cancer interaction (**Figure 3**).

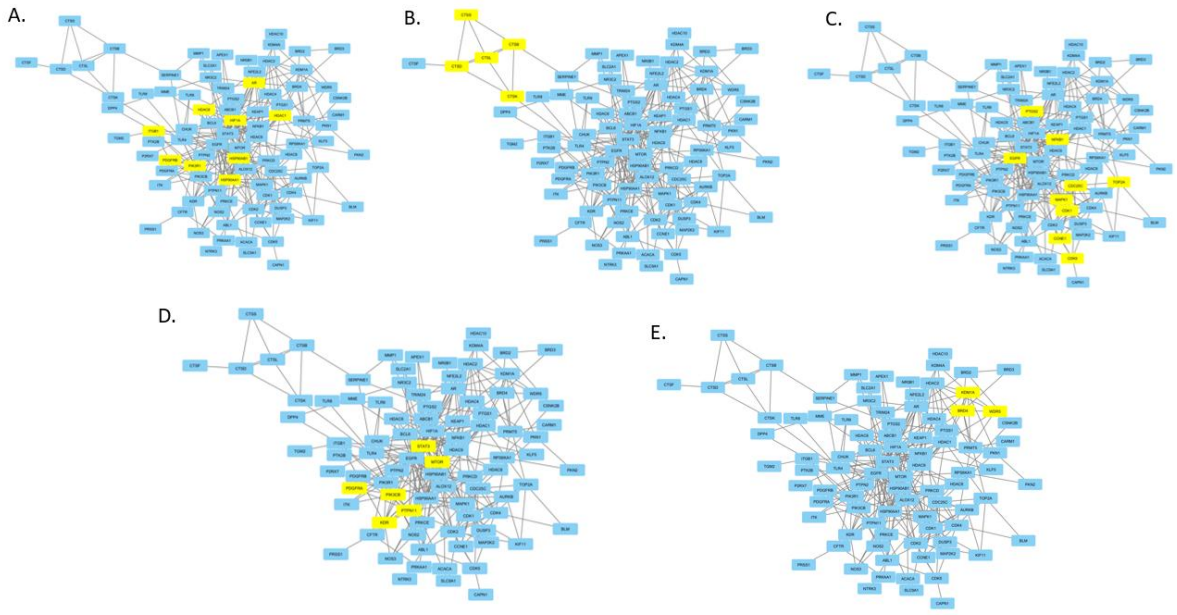


**Figure 3**. Protein clusters in the network identified using the MCODE algorithm: a) Cluster 1, b) Cluster 2, c) Cluster 3, d) Cluster 4, e) Cluster 5

Degree centrality (DC) quantifies the number of direct interactions for each protein and identifies highly connected nodes (Ashtiani et al., 2018). Closeness centrality (CC) and betweenness centrality (BC) provide additional measures of network importance. BC reflects a protein's influence over communication pathways, whereas CC estimates the efficiency of information flow (Ashtiani et al., 2018). Network topology analysis conducted with the Network Analyzer tool in Cytoscape identified STAT3, EGFR, HSP90AA1, HSP90AB1, HIF1A, HDAC1, TLR4, NFKB1, PIK3R1, and PTGS2 as the

top 10 proteins with the highest DC, CC, and BC values (**Table 5**). These results highlight the most influential regulatory nodes within the Peronemin–cervical cancer interaction network and propose these proteins as primary candidates for subsequent mechanistic and experimental studies.

MCODE analysis identified five densely connected protein clusters within the PPI network. This suggests the presence of functionally coherent modules (**Table 6**; **Figure 3**). Clusters 1 and 2 exhibited the highest MCODE scores (4.5), indicating strong internal connectivity. Cluster 1 included proteins involved in hypoxia response, signal transduction, and epigenetic regulation. Examples are HIF1A, HDACs, HSP90 isoforms, and PIK3R1, highlighting their potential roles in cancer cell adaptation and survival. Cluster 2 primarily consisted of cathepsin family members, which are associated with proteolytic activity and tumor invasion processes. Clusters 3 and 4 were enriched with proteins related to cell cycle regulation and oncogenic signaling pathways. These included CDKs, MAPK1, EGFR, STAT3, and components of the PI3K–mTOR axis. This underscores their relevance to cervical cancer proliferation and progression. Cluster 5 contained epigenetic regulators involved in chromatin remodeling. This suggests an additional layer of transcriptional control within the network. Collectively, these clusters reflect the multifaceted molecular mechanisms that may be modulated by Peronemin in cervical cancer.

**Table 5.** Top 10 Centrality Score (DC, CC, & BC)

| Filtered Nodes | Betweenness Centrality | Closeness Centrality | Degree |
|---|---|---|---|
| STAT3 | 0.211521545 | 0.535714286 | 29 |
| EGFR | 0.171100285 | 0.529411765 | 28 |
| HSP90AA1 | 0.126127876 | 0.526315789 | 27 |
| HSP90AB1 | 0.096027252 | 0.517241379 | 24 |
| HIF1A | 0.05880132 | 0.486486486 | 20 |
| HDAC1 | 0.061187203 | 0.459183673 | 19 |
| TLR4 | 0.167793038 | 0.454545455 | 15 |
| NFKB1 | 0.050167462 | 0.481283422 | 15 |
| PIK3R1 | 0.021924516 | 0.456852792 | 14 |
| PTGS2 | 0.075723268 | 0.447761194 | 11 |

**Table 6**. MCODE algorithm–based protein clusters

| Cluster | Score | Nodes | Node IDs |
|---|---|---|---|
| 1 | 4.5 | 9 | HIF1A, HDAC1, HSP90AA1, PIK3R1, PDGFRB, HSP90AB1, AR, ITGB1, HDAC6 |
| 2 | 4.5 | 5 | CTSL, CTSB, CTSD, CTSS, CTSK |
| 3 | 3.75 | 9 | CDK5, NFKB1, MAPK1, CDK1, CDC25C, EGFR, CCNE1, TOP2A, PTGS2 |
| 4 | 3.6 | 6 | PIK3CB, MTOR, KDR, STAT3, PTPN11, PDGFRA |

| | | | |
|---|---|---|---|
| 5 | 3 | 3 | BRD4, KDM1A, WDR5 |

In addition to classical centrality measures and MCODE analysis, the Maximal Clique Centrality (MCC) algorithm implemented in CytoHubba was applied to identify hub proteins within the PPI network. Hub proteins are defined as highly connected nodes with dense interactions among network components. Based on MCC scores, the top 10 hub proteins were AR, HSP90AA1, PIK3R1, PDGFRB, STAT3, EGFR, HDAC1, HIF1A, HSP90AB1, and NFKB1 (**Figure 4(a)**, **4(b)**).

STAT3 (Signal Transducer and Activator of Transcription 3) is a key protein node identified in the consensus of MCODE, CytoHubba, and Network Analyzer, making it a critical target for further study in cervical cancer. STAT3 plays a central role in regulating LC3B, a major autophagy biomarker that can either promote or inhibit cancer progression. Overexpression of STAT3 in cervical cancer tissues negatively correlates with LC3B levels. Knockout or knockdown of STAT3 enhances autophagy and reduces proliferation, migration, colony formation, and subcutaneous tumorigenesis of cervical cancer cells in vitro and in vivo. STAT3 mediates autophagy via the Bcl2–Beclin1 complex, with Bcl2 positively and Beclin1 negatively correlating with STAT3 expression, highlighting its involvement in this regulatory pathway. Thus, STAT3 represents a promising prognostic and therapeutic target (Wu et al., 2022).

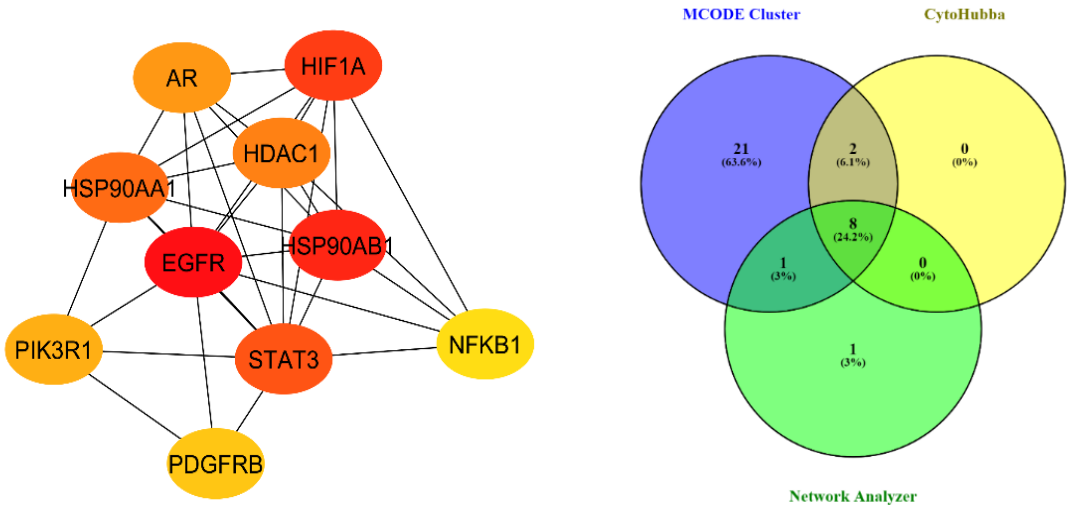


**(a)** **(b)**

**Figure 4.** (a) Top 10 hub proteins determined by CytoHubba Maximal Clique Centrality (MCC), (b) Venn diagram showing proteins identified by MCODE clusters, CytoHubba, and Network Analyzer

*3.6. Functional Analysis*

Gene Ontology (GO) analysis of biological processes indicated that genes targeted by Sungkai bioactive compounds are involved in multiple cancer-related processes (**Figure 5**). Among the most significantly enriched processes (FDR < 0.01) were regulation of gene expression, cell proliferation, inflammatory response, and apoptosis. Notably, STAT3 emerged as a key gene

associated with several enriched biological processes, including positive regulation of cell proliferation, inflammatory response, transcription from RNA polymerase II promoters, DNA-templated transcription, and positive regulation of interleukin-8 production.

These results are consistent with accumulating evidence highlighting the pivotal role of STAT3 in cervical cancer pathogenesis. As discussed above, STAT3 overexpression has been shown to promote cancer cell proliferation and survival while negatively regulating LC3B-mediated autophagy. Its involvement in transcriptional regulation and inflammatory signaling further underscores its central role in tumor progression. Accordingly, the present results suggest that Sungkai bioactive compounds may exert anticancer effects, at least in part, through modulation of STAT3 activity. By targeting STAT3 and associated signaling pathways, these bioactives may contribute to the suppression of cell proliferation, induction of apoptosis, and regulation of inflammatory responses, supporting their potential as multitarget anticancer agents.

Nevertheless, as this study is based on *in silico* predictions, experimental validation is required to confirm the anticancer mechanisms and safety profiles of these compounds.

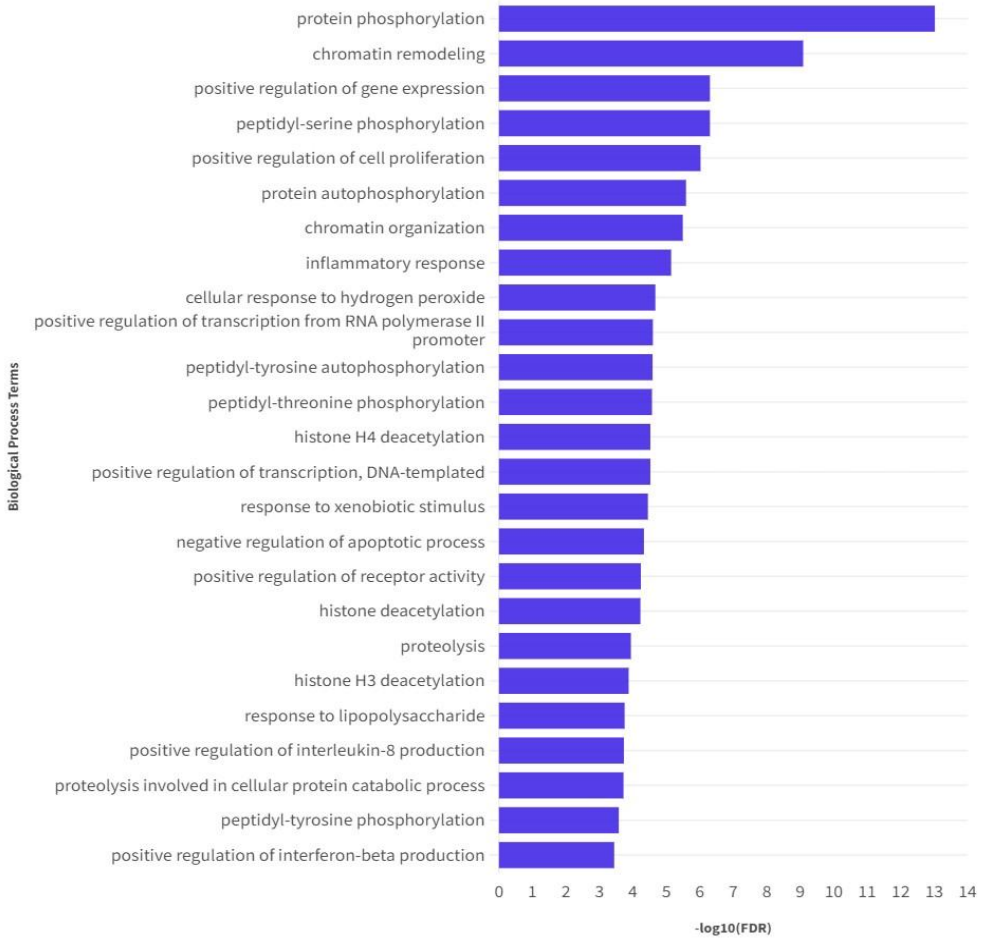


**Figure 5**. Top 25 Biological Process Gene Ontology Annotation FDR < 0.01

## 4. CONCLUSIONS

This study highlights peronemin derivatives, particularly C1 and D1, as previously underexplored natural scaffolds with multitarget potential against cervical cance. In silico predictions suggest they have low toxicity and are effective at stopping the growth of cervical cancer cells. Protein interaction analyses identified STAT3, EGFR, HSP90AA1, and HSP90AB1 as key targets of these compounds, with STAT3 being especially important for controlling cell growth, cell death, and inflammation in cervical cancer. Further analysis showed that these compounds affect several key cancer pathways, which supports their potential as drugs that can target multiple aspects of cancer. These results provide a solid scientific foundation for developing Sungkai-based compounds as potential new treatments for cervical cancer.

## ACKNOWLEDGMENT

The authors would like to thank Universitas Jambi for financial support for this research through the DIPA-PNBP of the Faculty of Science and Technology under the Community Service (PPM) scheme of Jambi University, No. 023.17.2.677565/2024 dated 24 November 2023, and the research agreement/contract No. 259/UN21.11/PT.01.05/SPK/2024 dated 14 June 2024.

## LIST OF REFERENCES

Ashtiani, M., Salehzadeh-Yazdi, A., Razaghi-Moghadam, Z., Hennig, H., Wolkenhauer, O., Mirzaie, M., & Jafari, M., (2018). A systematic survey of centrality measures for protein-protein interaction networks. *BMC systems biology*, *12*(1), 1-17.

Chin, C. H., Chen, S. H., Wu, H. H., Ho, C. W., Ko, M. T., & Lin, C. Y., (2014). cytoHubba: identifying hub objects and sub-networks from complex interactome. *BMC systems biology*, *8*(4), 1-7.

Coudert, E., Gehant, S., de Castro, E., Pozzato, M., Baratin, D., Neto, T., Sigrist, C.J., Redaschi, N. and Bridge, A., (2023). Annotation of biologically relevant ligands in UniProtKB using ChEBI. *Bioinformatics*, 39(1), p.btac793.

Daina, A., Michielin, O. and Zoete, V., (2019). SwissTargetPrediction: updated data and new features for efficient prediction of protein targets of small molecules. *Nucleic acids research*, 47(W1), pp.W357-W364.

Dong J, Wang NN, Yao ZJ, Zhang L, Cheng Y, Ouyang D, Lu AP, Cao DS. (2018). ADMETlab: a platform for systematic ADMET evaluation based on a comprehensively collected ADMET database. *Journal of cheminformatics*.10:1-1.

Filimonov D.A., Lagunin A.A., Gloriozova T.A., Rudik A.V., Druzhilovskii D.S., Pogodin P.V., Poroikov V.V. (2014). Prediction of the biological activity spectra of organic compounds using the PASS online web resource. *Chemistry of Heterocyclic Compounds*, 50 (3), 444-457.

Gilson,M.K., Liu,T., Baitaluk,M., Nicola,G., Hwang, L. and Chong,J. (2015). BindingDB in 2015: A public database for medicinal chemistry, computational chemistry and systems pharmacology. *Nucleic Acids Research* 44:D1045-D1053.

Hull R, Mbele M, Makhafola T, Hicks C, Wang SM, Reis RM, Mehrotra R, Mkhize-Kwitshana Z, Kibiki G, Bates DO, Dlamini Z., (2020). Cervical cancer in low and middle-income countries. doi: 10.3892/ol.2020.11754. PMID: 32782524; PMCID: PMC7400218.

Kohut, A., Martincuks, A., Santiago, N.L., Austria, T., Zhao, Q., Lee, S., Tergas, A., Dellinger, T., Han, E., Rodriguez-Rodriguez, L. and Yu, H., (2022). STAT3 is a potential therapeutic target in cervical cancer (257). *Gynecologic Oncology*, *166*, pp.S137-S138.

Lagunin A.A., Dubovskaja V.I., Rudik A.V., Pogodin P.V., Druzhilovskiy D.S., Gloriozova T.A., Filimonov D.A., Sastry G.N., Poroikov V.V. CLC-Pred: a freely available web-service for in silico prediction of human cell line cytotoxicity for drug-like compounds. *PLOS One*, 2018, 13 (1), e0191838. DOI: 10.1371/journal.pone.0191838

Lee HG, Yu KA, Oh WK, Baeg TW, Oh HC, Ahn JS, Jang WC, Kim JW, Lim JS, Choe YK, Yoon DY.,(2005) Inhibitory effect of jaceosidin isolated from Artemisiaargyi on the function of E6 and E7 oncoproteins of HPV 16. *J Ethnopharmacol*. doi: 10.1016/j.jep.2005.01.054. PMID: 15814270.

Malikhana, Yuniastuti. Susanti, R., &WH, N., (2021).Studi In Silico potensi senyawa bioaktif gembili (Dioscorea esculenta) sebagai ligan pada reseptor G6PD dan PTPN1. *Prosiding Semnas Biologi* ke 9, 29-34.

Morgan, E.L. and Macdonald, A., (2019). Autocrine STAT3 activation in HPV positive cervical cancer through a virus-driven Rac1—NFκB—IL-6 signalling axis. *PLoS pathogens*, *15*(6), p.e1007835.

Nageen B, Rasul A, Hussain G, Shah MA, Anwar H, Hussain SM, Uddin MS, Sarfraz I, Riaz A, Selamoglu Z.,(2021) Jaceosidin: A Natural Flavone with Versatile Pharmacological and Biological Activities. *Curr Pharm*;27(4):456-466. doi: 10.2174/1381612826666200429095101. PMID: 32348212.

Nickel J, Gohlke BO, Erehman J, Banerjee P, Rong WW, Goede A, Dunkel M, Preissner R.,(2014) SuperPred: update on drug classification and target prediction. *Nucleic Acids Res*. PMID: 24878925; PMCID: PMC4086135.

Nikolaou M, Pavlopoulou A, Georgakilas AG, Kyrodimos E., (2018). The challenge of drug resistance in cancer treatment: a current overview. *Clin Exp Metastasis*. 35(4):309-318. doi: 10.1007/s10585-018-9903-0. Epub 2018 May 24. PMID: 29799080.

Piñero, J., Ramírez-Anguita, J.M., Saüch-Pitarch, J., Ronzano, F., Centeno, E., Sanz, F. and Furlong, L.I., 2020. The DisGeNET knowledge platform for disease genomics: 2019 update. *Nucleic acids research*, 48(D1), pp.D845-D855.

Pogodin, P.V., Lagunin, A.A., Filimonov, D.A. and Poroikov, V.V., 2015. PASS Targets: Ligand-based multi-target computational system based on a public data and naïve Bayes approach. *SAR and QSAR in Environmental Research*, 26(10), pp.783-793.

Stelzer, G., Rosen, N., Plaschkes, I., Zimmerman, S., Twik, M., Fishilevich, S., Stein, T.I., Nudel, R., Lieder, I., Mazor, Y. and Kaplan, S., 2016. The GeneCards suite: from gene data mining to disease genome sequence analyses. *Current protocols in bioinformatics*, 54(1), pp.1-30.

Wu, L., Shen, B., Li, J., Zhang, H., Zhang, K., Yang, Y., Zu, Z., Shen, D. and Luo, M., 2022. STAT3 exerts pro-tumor and anti-autophagy roles in cervical

cancer. *Diagnostic Pathology*, *17*(1), pp.1-10.

Xiong G, Wu Z, Yi J, Fu L, Yang Z, Hsieh C, Yin M, Zeng X, Wu C, Lu A, Chen X.,(2021) ADMETlab 2.0: an integrated online platform for accurate and comprehensive predictions of ADMET properties. *Nucleic Acids Research*.

Yao, Z.J., Dong, J., Che, Y.J., Zhu, M.F., Wen, M., Wang, N.N., Wang, S., Lu, A.P. and Cao, D.S., (2016). TargetNet: a web service for predicting potential drug–target interaction profiling via multi-target SAR models. *Journal of computer-aided molecular design*, 30, pp.413-424.

JURNAL ILMIAH BERKALA SAINS DAN TERAPAN KIMIA
**Jurnal Ilmiah Berkala: Sains dan Terapan Kimia**
*Vol. 20 No. 1, January 2026*

# Analysis of Atmospheric Vertical Structure During Hail in Tangerang: A Comparative Study of ECMWF Model Data and Radiosonde Observations

# Analisis Struktur Vertikal Atmosfer Saat Hujan Es Di Tangerang: Studi Komparasi Data Model ECMWF dan Observasi Radiosonde

**Dhanu Prakoso[1*], Aries Kristianto[1]**

[1]Program Studi Meteorologi, Sekolah Tinggi Meteorologi Klimatologi dan Geofisika, Jalan Meteorologi 5 Tanah Tinggi, Tangerang, 15221, Indonesia

Email: dhanuprakoso07@gmail.com

**ABSTRACT**

*Hail is an extreme weather event in tropical regions with local characteristics, short duration, and difficult to predict precisely. The hail event in Tangerang on October 31, 2025, is an important anomaly to study in order to understand the atmospheric structure that triggers massive instability in urban areas. This study aims to identify the vertical conditions of the atmosphere through a comparative study between global numerical model data from the European Centre for Medium-Range Weather Forecasts (ECMWF) and in-situ Radiosonde observation data. The methodology used is a case study approach by integrating remote sensing data from the Himawari-9 Satellite and C-Band Weather Radar to validate the structure of storm cells. Thermodynamic parameters such as Convective Available Potential Energy (CAPE) and freezing level profiles are extracted using Python programming to evaluate the model's ability to represent atmospheric lability conditions. The research results show a "wet bias" in the model data, indicating that the model is more humid than actual conditions.*

**Keywords** Hail; radar; radiosonde; ECMWF

**Received**: 22 December 2025 ; **Accepted**: 23 January 2026: **Available online**: 29 January 2026

## 1. INTRODUCTION

Indonesia, as an archipelagic country located in the equatorial region, has unique weather characteristics with intense solar heating throughout the year. One of the extreme weather phenomena that often occurs during the transition period (*pancaroba*) in this region is hail. By definition, hail is a form of precipitation consisting of balls or irregular lumps of ice, caused by strong convective systems with updrafts exceeding the terminal velocity of ice particles (Knight & Knight, 2001). Unlike in mid-latitudes, the high freezing level in the tropics (typically > 4.5 km) acts as a deep melting layer, implying that only storms with intense updrafts and large initial hailstones can produce surface hail (Taszarek et al., 2021).

Hailstorms in the tropics are often very localized, short-lived, and challenging to

predict. The formation of hail requires specific atmospheric ingredients, namely significant conditional instability, sufficient moisture, and a favorable freezing level height that allows ice to reach the surface before melting. In tropical environments, these storms are typically driven by convective systems with vigorous updrafts capable of supporting heavy hydrometeors. Recent observations indicate that the impact of such storms is increasingly significant in populated urban areas due to changing environmental conditions.

Recently, a significant hail event struck the Tangerang region in Banten on October 31, 2025. This event mirrors similar convective occurrences in Java, where rapid cloud growth and temperature drops are key precursors. Based on community reports and radar observations, the hail event was highly localized, specifically impacting the Gading Serpong area (Kelapa Dua District) and extending to the Jelupang area (North Serpong District). Reports indicated hail accompanied by strong winds causing significant impacts in these densely populated zones (Tristiawati, 2025). This incident is particularly notable as it occurred in a developed urban area, where the Urban Heat Island (UHI) effect can locally enhance convective initiation and storm intensity.

Operational mitigation of hail relies heavily on early detection and atmospheric profiling. Doppler Weather Radar is the primary tool for detecting high-reflectivity cores associated with hail. Furthermore, satellite imagery from Himawari-8/9 allows for the detection of overshooting tops and cloud top cooling, which are signatures of severe updrafts penetrating the tropopause (Bessho et al., 2016). However, remote sensing alone cannot fully resolve the thermodynamic environment, such as the vertical distribution of temperature and humidity, which determines the potential for ice growth and melting.

To characterize the vertical atmospheric profile, radiosonde observations are widely considered the gold standard for in-situ upper-air measurements. However, the spatial and temporal scarcity of radiosonde launches limits their utility for capturing localized storms. Consequently, numerical weather prediction (NWP) models, such as the ERA5 reanalysis and forecasts from the European Centre for Medium-Range Weather Forecasts (ECMWF), are essential for filling these observational gaps (Hersbach et al., 2020). Nevertheless, discrepancies between global models and tropical observations persist. Previous studies, such as Mulsandi et al. (2021), highlight that reanalysis data often exhibit moisture biases and may smooth out extreme instability gradients in the tropics, necessitating rigorous validation against local soundings.

Therefore, this study aims to identify the vertical atmospheric conditions associated with the hail event in Tangerang on 31 October 2025 through a comparative analysis. While previous studies have focused on general radar characteristics or climatology, there is a lack of quantitative evaluation regarding how well the ECMWF model represents the specific hail-favoring profiles, specifically freezing level and CAPE, in an Indonesian urban setting. This study compares ECMWF profiles with radiosonde observations and validates them against radar data to determine the model's reliability and understanding of the storm's thermodynamic drivers.

## 2. MATERIALS AND METHODS

### *2.1. Materials*

The main datasets used in this study consist of remote sensing data and atmospheric observation data. Himawari-9 satellite infrared imagery (Channel 13) and C-band weather radar data were obtained from the

Meteorology Directorate of the Indonesian Agency for Meteorology, Climatology, and Geophysics (BMKG). Upper-air observation data were derived from radiosonde soundings obtained from the University of Wyoming database, corresponding to station ID 96749 (Soekarno–Hatta Meteorological Station), located at 6.24°S and 106.63°E. Radiosonde observations at 00 and 12 UTC were used.

Global model data were obtained from the ERA5 reanalysis dataset produced by the European Centre for Medium-Range Weather Forecasts, accessed through the Climate Data Store platform. ERA5 pressure-level data with a horizontal resolution of 0.25° × 0.25° (~30 km) were extracted at grid points nearest to the radiosonde station location for 00 and 12 UTC on 31 October 2025.

Convective instability was assessed using mixed-layer Convective Available Potential Energy (MLCAPE), defined as the parcel averaged over the lowest 50 hPa of the atmosphere. Radiosonde profiles were vertically interpolated to standard pressure levels to match ERA5 data using linear interpolation. Model performance was quantitatively evaluated using bias and root mean square error between ERA5 and radiosonde-derived parameters, including freezing level height, lapse rate, and MLCAPE.

### *2.2. Methods*

This study uses a case study approach by integrating remote sensing data and numerical models. Data processing is performed computationally using Python programming scripts on the Google Colab platform. Specifically, the MetPy library was utilized to extract and visualize atmospheric parameters such as pressure, temperature, dew point, and wind profiles (May et al., 2022). These parameters are then analyzed to calculate the atmospheric stability index and generate vertical profiles (Skew-T Log-P diagrams). The level of atmospheric instability was analyzed based on the Convective Available Potential Energy (CAPE) value, which refers to the classification standard established by the National Weather Service (n.d.), as shown in Table 1. In addition, the storm cell structure was validated using the Column Maximum (CMAX) and Vertical Cut (VCUT) products from radar data processed using Rainbow® 5 software (Leonardo Germany GmbH, 2018). The analysis method focused on a comparative test between the ECMWF model thermodynamic profile and in-situ observation data (radiosonde) to evaluate the accuracy of the model in representing atmospheric instability conditions (**Table 1**).

**Table 1.** CAPE Classification (Data Source: National Weather Service)

| CAPE (J/kg) | Instability Level |
|---|---|
| < 1000 | Weak Instability |
| 1000 – 2500 | Moderate Instability |
| 2500 – 4000 | Strong Instability |
| > 4000 | Extreme Instability |

## 3. RESULTS AND DISCUSSION

This section presents the results of an analysis of meteorological conditions and the vertical structure of the atmosphere during the hailstorm in Tangerang on October 31, 2025.

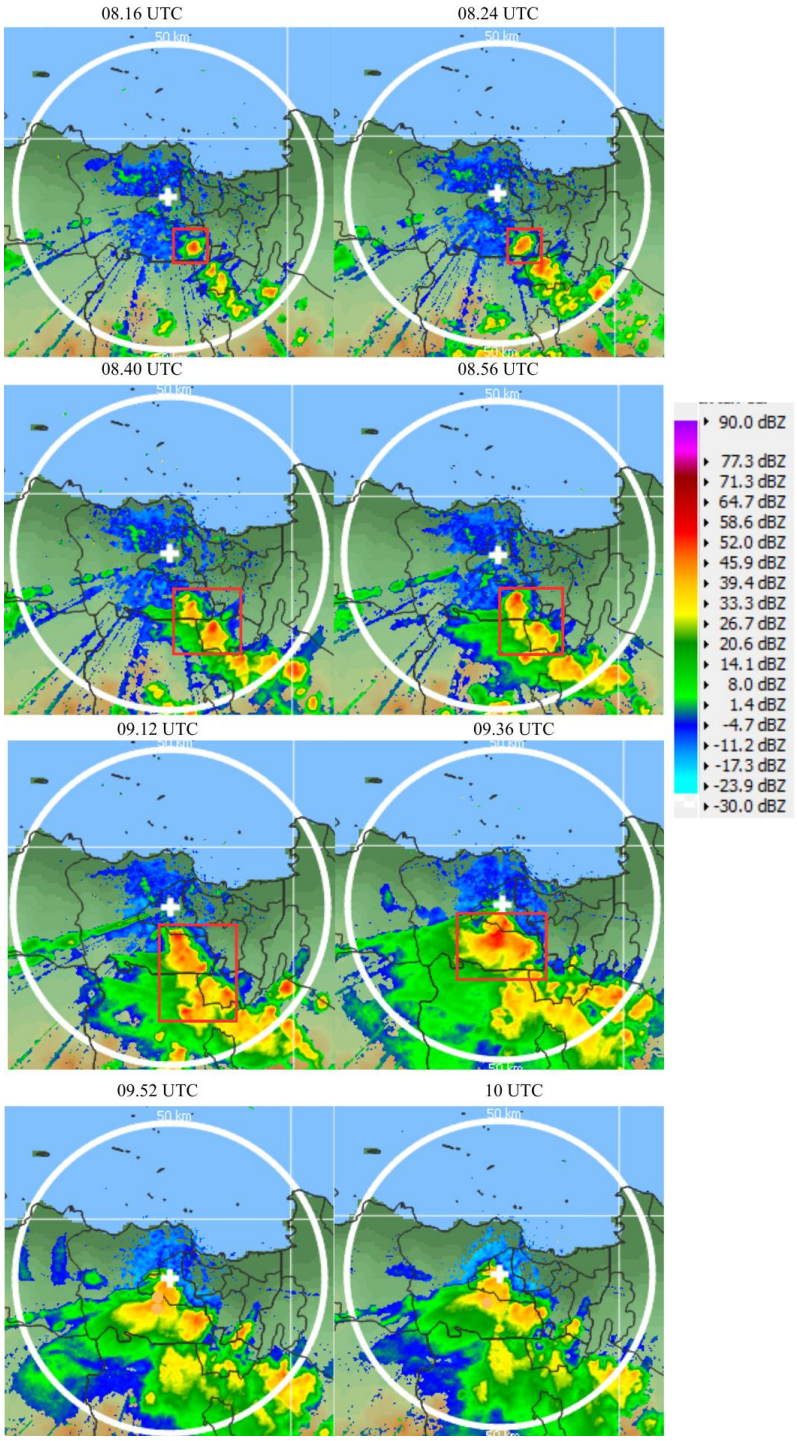


**Figure 1**. Tangerang Radar CMAX Product

The discussion covers the spatial and temporal evolution of convective clouds based on radar and satellite imagery, as well as a comparison of thermodynamic profiles between observational data and numerical models to understand the instability mechanisms that occurred. Analysis of storm cell evolution based on C-Band radar reflectivity (**Figure 1**) shows a maximum value exceeding 50 dBZ in the storm core moving from Depok to Tangerang. Physically, this high reflectivity value indicates the presence of large solid hydrometeors (ice grains) that trigger strong radar wave backscattering (Mie scattering). This is in line with the findings of Ardiansyah (2022) in the Meteorology, Climatology, and Geophysics Bulletin, which states that radar reflectivity values of up to 60 dBZ are a strong indicator of the mature phase of clouds causing hail. This indication of explosive cloud growth is reinforced by data from the Himawari-9 satellite, which detected a Cloud Top Temperature reaching -80°C. This extreme cooling indicates an overshooting top that penetrates the tropopause, as explained by Nugraha and Fadlan (2018), who found that cloud top temperatures below -77°C have a significant correlation with hail occurrences in tropical regions.

From a thermodynamic perspective, although the CAPE value is moderate, this event is significantly influenced by the freezing level altitude. According to Fadholi (2013) in the Indonesian Journal of Physical Sciences, even though Indonesia has a relatively higher freezing level compared to mid-latitudes, hail can still reach the surface if supported by strong downdrafts and high humidity, which prevent the ice grains from melting completely. Finally, validation of global model data against in-situ observations shows that the model tends to underestimate the peak instability index. This bias is consistent with the study by Mulsandi et al. (2021) who evaluated model performance in Indonesia, where model/reanalysis data often has limitations in capturing extreme values of local-scale convective parameters, but still represents atmospheric spatial and temporal patterns quite well.

**Figure 2** shows the results of VCUT Radar, which displays the vertical conditions of the atmosphere. The time selected is when hail occurred in the Tangerang area, which was at 09:36 UTC or 16:36 WIB. At an altitude of between 2 and 4 km, which is the freezing level, there was high reflectivity of >50 dBZ. This indicates the presence of ice crystals formed at that altitude.

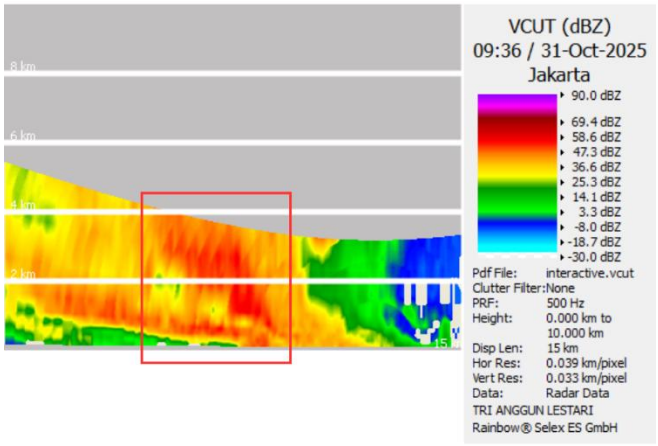


**Figure 2.** Tangerang Radar VCUT Product

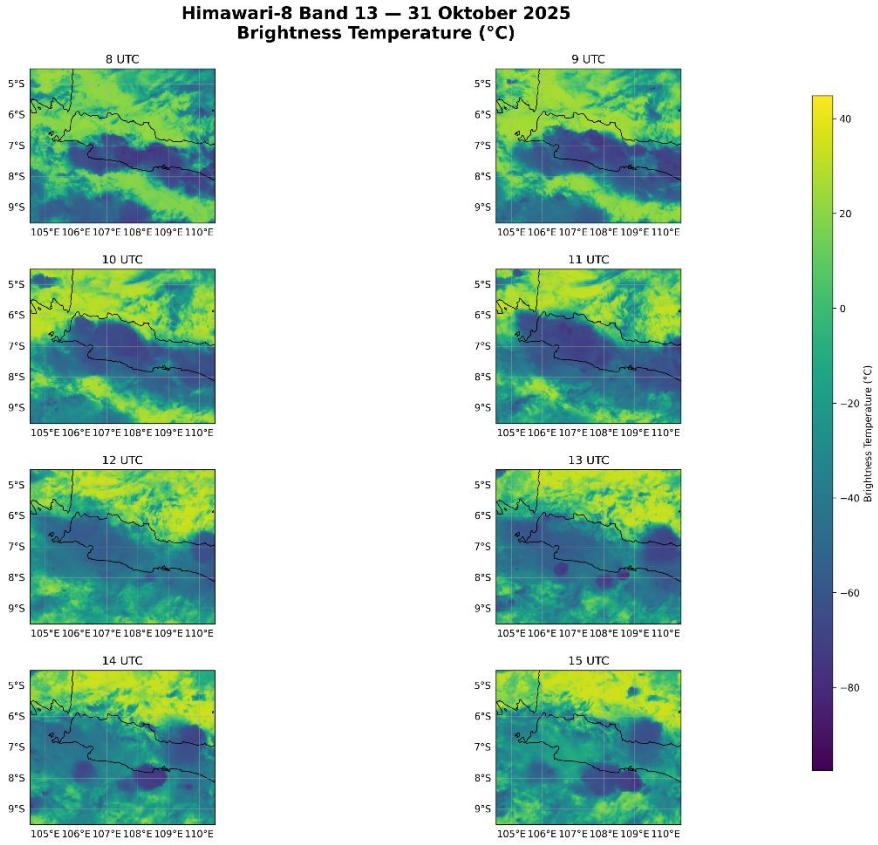


**Figure 3**. Peak Cloud Temperature Development Throught Satellite Images

**Figure 3.** illustrates the spatial distribution of the minimum brightness temperature observed during the hailstorm in Tangerang. At 08:00 UTC, convective clouds with extremely cold cloud tops were observed stretching from the southern to the central region of West Java. From 09:00 UTC to 13:00 UTC, the system intensified and expanded, covering the entire West Java region, including Tangerang.

The cloud top temperature reached approximately -60 °C. This significant temperature drop indicates a rapid vertical development penetrating the tropopause layer. Such extreme cooling corresponds to the Overshooting Top (OT) signature, which is statistically strongly correlated with severe weather events, including hail and damaging winds (Bedka et al., 2010).

Evaluation of the atmospheric vertical profiles at 00 UTC (**Figure 4**) and 12 UTC (**Figure 5**) provides crucial insights into the performance of the ECMWF model and the physical mechanisms of hail formation. At 00 UTC, data comparison shows that although the model is able to represent the lower-layer moisture structure well, it tends to underestimate the intensity of thermodynamic instability (CAPE) compared to in-situ observations.

This bias is a consequence of the global model resolution that averages local-scale convective parameters, where reanalysis data in the tropics often suffers from a wet bias but fails to capture the sharp temperature lapse rate, as explained in the model evaluation by Mulsandi et al. (2021). Despite the quantitative discrepancy reflected in the RMSE values, the qualitative agreement of the

vertical profile patterns confirms that the model remains valid for identifying pre-convective environments, as the bias does not eliminate the key physical signal of massive water vapor availability. Furthermore, analysis at 12 UTC during the mature phase of the storm revealed that this hail event formed under moderate CAPE conditions, in contrast to the characteristics of subtropical storms which are generally triggered by extreme instability energy.

The success of hail formation under these moderate energy conditions was predominantly controlled by the observed freezing level height at 4.8 km. Referring to the findings of Fadholi (2013), a freezing level height in the range of 4–5 km is an ideal condition in the Indonesian region that allows ice grains to have sufficient residence time in the cold layer to grow, as well as a short enough fall distance to reach the ground surface without melting completely, supported by a thick moisture profile (deep moisture) that protects the updraft column from dry air entrainment.

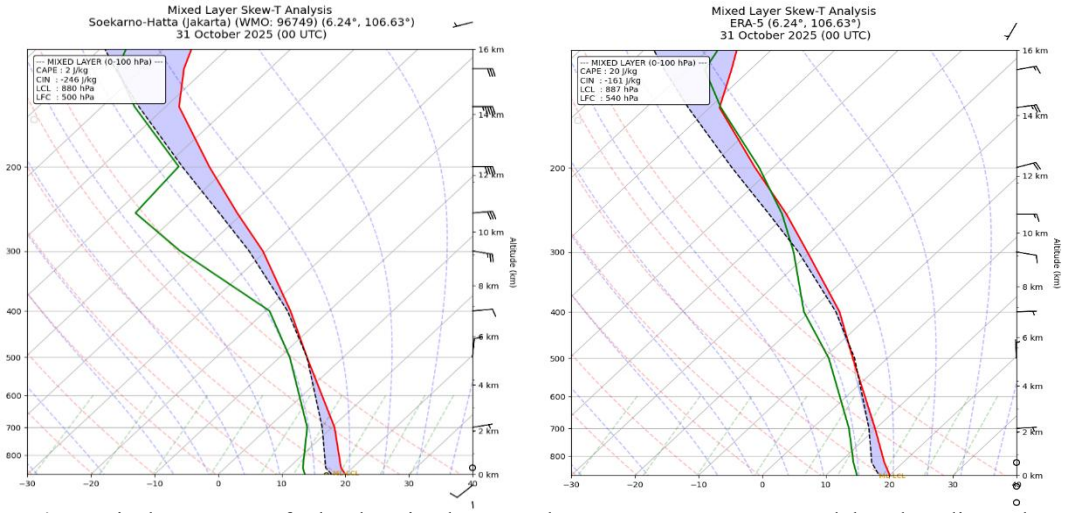


**Figure 4**. Vertical Structure of Clouds Mixed Layer Skew-T Data ECMWF Model and Radiosonde Data 00 UTC

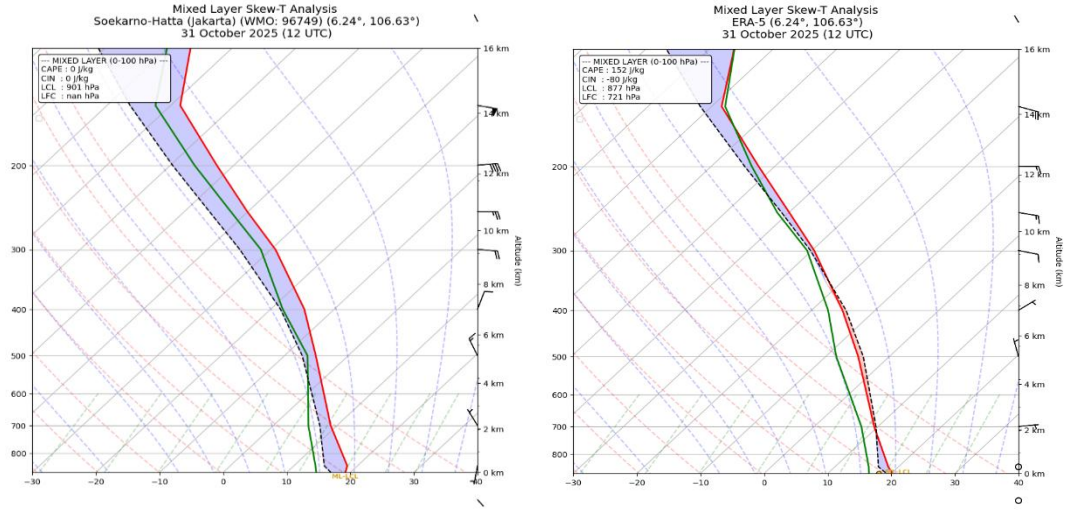


**Figure 5.** Vertical Structure of Clouds Skew-T Log-P Data ECMWF Model and Radiosonde Data 12 UTC

**Table 1.** Bias and RMSE Values of Temperature and Dewpoint Parameters between Model and Radiosonde Data at 00 UTC and 12 UTC

| Time | Temperature Bias | RMSE Temperature | Bias Dewpoint | RMSE Dewpoint |
|---|---|---|---|---|
| 00 UTC | 0,277401924 | 0,952667642 | 3,603164291 | 6,375474701 |
| 12 UTC | 0,565832825 | 1,591942278 | 1,666738281 | 2,398636698 |

A comparative analysis of the atmospheric profiles in **Figures 4.** (00 UTC) and **Figure 5.** (12 UTC) shows characteristic differences between the ECMWF model predictions and radiosonde observational data. At 00 UTC, the model predicts a higher convective energy (CAPE) value than the observational data. The primary cause of this discrepancy is confirmed through statistical evaluation in **Table 1.** which shows a dewpoint bias of +3.60°C. This positive bias indicates that the model estimates atmospheric conditions that are much more humid than actual conditions, directly causing an overestimation of potential storm energy. This phenomenon of overestimated humidity in the model in tropical regions is consistent with the findings of Mulsandi et al. (2021). In addition to model bias, differences in data collection locations between Soekarno-Hatta Airport (for observations) and the event point in South Tangerang (for the model) also contribute to this variation, given the highly localized nature of convective clouds.

Furthermore, at 12 UTC during the mature phase of the storm, the decrease in humidity bias to +1.67°C in **Table 1.** is followed by observational data indicating that hail formed under conditions of moderate, rather than extreme, instability. This proves that hail formation in the study area does not solely depend on the magnitude of CAPE energy. Referring to Fadholi (2013), the determining factor for hail success in this case is the freezing level altitude, which is at 4.8 km. This altitude is ideal because it provides sufficient time for ice grains to grow, but the fall distance is short enough to prevent complete melting before reaching the surface. Thus, despite differences in quantitative values due to humidity bias and location, both datasets qualitatively successfully identify the saturated atmospheric structure that supports storm cloud growth.

## 4. CONCLUSION

The analysis of the hail event in Tangerang reveals that deep convection in tropical environments can produce severe weather even under conditions of limited thermodynamic instability. Remote sensing analysis confirmed the severity of the storm cell, where C-Band Weather Radar detected reflectivity values exceeding 50 dBZ and Himawari-9 satellite imagery observed Cloud Top Temperatures reaching -80°C, signifying large hydrometeors and vigorous updraft penetration. Thermodynamically, the event was driven not by extreme instability—as indicated by negligible Radiosonde CAPE (0–2 J/kg) and weak ECMWF model instability (20–152 J/kg)—but rather by a favorable freezing level at 4.8 km and deep moisture availability that sustained the ice phase despite significant convective inhibition. A comparative evaluation highlights a distinct "wet bias" in the ECMWF model, characterized by a positive dewpoint bias of +3.60°C at 00 UTC, which led to an overestimation of instability compared to in-situ soundings: a discrepancy attributed to global model limitations in resolving local humidity and spatial differences between grid points. Consequently, operational forecasting in Indonesia should not rely solely on high CAPE thresholds but must integrate radar signatures with freezing level monitoring,

while future research should address the limitations of coarse global models by utilizing high-resolution mesoscale models (e.g., WRF) to better resolve the explicit microphysical processes of tropical hail.

**ACKNOWLEDGMENT**

The author would like to express his sincere gratitude to the University of Wyoming and the European Centre for Medium-Range Weather Forecasts (ECMWF) for providing access to radiosonde data and ERA5 reanalysis data that were essential for the completion of this study. The author also thanks the Sekolah Tinggi Meteorologi, Klimatologi, dan Geofisika (STMKG) as the institution where the author studied, for providing the facilities and a conducive academic environment that enabled this research to be completed successfully.

**LIST OF REFERENCES**

Ali, A., & Hidayati, S. (2015). Peringatan dini potensi hujan es menggunakan metode severe hail index berdasarkan pengamatan radar cuaca doppler. *Prosiding Seminar Nasional Fisika (E-Journal) SNF2015*, *4*, SNF2015-IX-25–SNF2015-IX-30.

Ali, A., & Sa'adah, U. (2022). Implementasi metode deteksi hujan es berbasis data radar cuaca menggunakan algoritma severe hail index (SHI). *Jurnal Fisika Unand*, *11*(3), 380–386. https://doi.org/10.25077/jfu.11.3.380-386.2022

Anggoro, M. D., & Pramujo, B. (2017). Kajian waktu hidup dan pergerakan awan konvektif berbasis citra radar dan model ECMWF. *Jurnal Meteorologi Klimatologi dan Geofisika*, *4*(3), 24–31.

Ardiansyah, D. (2022). Labilitas atmosfer terkait kejadian hujan es (Studi kasus hujan es di Sindang Dataran Bengkulu Tanggal 25 Juni 2021). *Buletin Meteorologi, Klimatologi, dan Geofisika*, *2*(2), 34–48.

Bedka, K., Brunner, J., Dworak, R., Feltz, W., Otkin, J., & Greenwald, T. (2010). Objective satellite-based detection of overshooting tops using infrared window channel brightness temperature gradients. *Journal of Applied Meteorology and Climatology*, *49*(2), 181–202. https://doi.org/10.1175/2009JAMC2286.1

Bessho, K., Date, K., Hayashi, M., Ikeda, A., Imai, T., Inoue, H., Kumagai, Y., Miyakawa, T., Murata, H., Ohno, T., Okuyama, A., Ozawa, R., Sakai, K., Shimoda, H., Shimoji, K., Tanaka, H., Yoshida, R., & Yoshino, R. (2016). An introduction to Himawari-8/9 Japan's new-generation geostationary meteorological satellites. *Journal of the Meteorological Society of Japan. Ser. II*, *94*, 151–183. https://doi.org/10.2151/jmsj.2016-009

Carminati, F., Migliorini, S., Ingleby, B., Bell, W., Lawrence, H., Newman, S., Hocking, J., & Smith, A. (2019). Using reference radiosondes to characterise NWP model uncertainty for improved satellite calibration and validation. *Atmospheric Measurement Techniques*, *12*, 83–106. https://doi.org/10.5194/amt-12-83-2019

Fadholi, A. (2013). Analisa kondisi atmosfer pada kejadian cuaca ekstrem hujan es (Hail). *Simetri: Jurnal Ilmu Fisika Indonesia*, *2*(1), 74–80.

Hersbach, H., Bell, B., Berrisford, P., Hirahara, S., Horányi, A., Muñoz-Sabater, J., Nicolas, J., Peubey, C., Radu, R., Schepers, D., Simmons, A., Soci, C.,

Abdalla, S., Abellan, X., Balsamo, G., Bechtold, P., Biavati, G., Bidlot, J., Bonavita, M., … Thépaut, J. N. (2020). The ERA5 global reanalysis. *Quarterly Journal of the Royal Meteorological Society*, *146*(730), 1999–2049. https://doi.org/10.1002/qj.3803

Hidayat, A. M., Efendi, U., & Rahmadini, H. N. (2017). Identifikasi kejadian hujan es berbasis analisis faktor cuaca, citra satelit dan model numerik dengan aplikasi GrADS (Studi kasus: kejadian hujan es tanggal 19 dan 23 April 2017 di Bandung). *Seminar Nasional Penginderaan Jauh ke-4 Tahun 2017*, 429–440.

Ingleby, B., Isaksen, L., Dahoui, M., Garcia-Mendez, A., & Gaffard, C. (2016). Improved radiosonde bias corrections in the ECMWF system. *Quarterly Journal of the Royal Meteorological Society*, *142*(696), 1664–1675. https://doi.org/10.1002/qj.2779

Knight, C. A., & Knight, N. C. (2001). Hailstorms. In C. A. Doswell III (Ed.), *Severe convective storms* (pp. 223–254). American Meteorological Society.

Leonardo Germany GmbH. (2018). *Rainbow® 5: The complete sensor analysis solution* [Computer software]. Leonardo. https://www.leonardocompany.com

May, R. M., Arms, S. C., Marsh, P., Bruning, E., Leeman, J. R., Goebbert, K., Thielen, J. E., & Bruick, Z. S. (2022). *MetPy: A Python package for meteorological data*. Unidata. https://doi.org/10.5065/D6WW7G29

Mulsandi, A., Sopaheluwakan, A., Faqih, A., Hidayat, R., & Koesmaryono, Y. (2021). Evaluasi performa indeks monsun AUSMI dan WNPMI di wilayah Indonesia. *Jurnal Sains & Teknologi Modifikasi Cuaca*, *22*(2), 75–84. https://doi.org/10.29122/jstmc.v22i2.4649

National Weather Service. (n.d.). *Severe weather topics: CAPE*. NWS Forecast Office Lincoln, IL. Retrieved December 22, 2025, from https://www.weather.gov/ilx/swop-severetopics-cape

Nugroho, A. D., & Fadlan, A. (2018). Analisis kejadian hujan es berdasarkan kondisi atmosfer dan citra satelit Himawari-8 (Studi kasus: Magelang, 24 Januari 2018). *Prosiding Seminar Nasional Meteorologi Klimatologi dan Geofisika*, 203–210.

Taszarek, M., Allen, J. T., Marchio, M., & Brooks, H. E. (2021). Global climatology and trends in convective environments from ERA5 and rawinsonde data. *npj Climate and Atmospheric Science*, *4*(1), 1–11. https://doi.org/10.1038/s41612-021-00190-x

Tristiawati, P. (2025, Oktober 31). *Hujan es terjadi sekitar 3 menit, pengunjung Mal Serpong sempat menghindar*. Liputan6.com. https://www.liputan6.com/news/read/6200251/hujan-es-terjadi-sekitar-3-menit-pengunjung-mal-serpong-sempat-menghindar

University of Wyoming. (2025). *Atmospheric soundings*. University of Wyoming College of Engineering. http://weather.uwyo.edu/upperair/sounding.html

JURNAL ILMIAH BERKALA SAINS DAN TERAPAN KIMIA

**Jurnal Ilmiah Berkala: Sains dan Terapan Kimia**
*Vol. 20 No. 1, January 2026*

# Performance Evaluation of Bentonite–Nano $SiO_2$ as an Adsorbent in the Decolorization Process of Rhodamine B

# Evaluasi Kinerja Bentonit–Nano $SiO_2$ sebagai Adsorben pada Proses Dekolorisasi Rhodamin B

**Regna Tri Jayanti[1], Miftahul Khairati[2], Enny Nurmalasari[2*], Puji Rahayu[3], Dennis Farina Nury[3], Okti Ulandari[1], Andhini Putri Trianita[3]**

[1]Renewable Energy Bioprocess Engineering Department, ATI Padang Polytechnic, Padang, West Sumatra, Indonesia (25171)
[2]Agro Chemical Engineering Department, ATI Padang Polytechnic, Padang, Sumatera Barat, Indonesia (25171)
[3]Industrial Process Technology Department, Petrochemical Industry Polytechnic of Banten, Jl. Raya Karang Bolong, Serang, Indonesia, 42166

Email: ennynurmalasari@poltekatipdg.ac.id

**ABSTRACT**

*Among various sources of industrial water pollution, effluents from printing, dyeing, and textile processes represent one of the most significant environmental threats. These wastewaters contain numerous toxic and hazardous substances that are difficult to biodegrade. This study investigates the synthesis, characterization, and adsorption performance of a Bentonite–Nano $SiO_2$ composite for the removal of Rhodamine B dye from aqueous solutions. The research was conducted in two main stages: the preparation of the Bentonite–Nano $SiO_2$ composite and the evaluation of its adsorption performance at various adsorbent concentrations and contact times. The composite was synthesized by dispersing nano-silica (15% w/w) into bentonite using ethanol as the solvent, followed by stirring, filtration, and drying processes. Characterization using Scanning Electron Microscopy (SEM) and Fourier Transform Infrared Spectroscopy (FTIR) confirmed successful modification. Adsorption tests showed that Rhodamine B removal efficiency increased with higher adsorbent concentration, reaching optimal conditions at 0.75% (w/v) with a removal efficiency of 90.2% after a contact time of 10–15 minutes. The enhanced adsorption performance was attributed to the larger surface area, higher porosity, and increased number of active sites resulting from the incorporation of nano-silica.*

**Keywords:** Bentonite–Nano $SiO_2$; adsorption; Rhodamine B; wastewater treatment

**Received**: 09 December 2025 ; **Accepted**: 09 January 2026: **Available online**: 29 January 2026

## 1. INTRODUCTION

Among the various sources of industrial water pollution, printing, dyeing, and textile effluent is one of the significant environmental threats. These wastewaters are high in many toxic and hazardous substances with low susceptibility to biodegradation (Małachowska et al., 2021). Dye containing effluents, especially, impose a significantly adverse effect on human health as well as the

natural environment (Kolya & Kang, 2024). Wastes of synthetic dyes such as Rhodamine B, methyl orange, Congo red, methylene blue, and tetracycline hydrochloride frequently consist of toxic chemical compounds such as nitrates, sulfur compounds, acetic acid, chromium species, and small quantities of heavy metals (e.g., arsenic, lead, mercury, cadmium, nickel, cobalt, and zinc). The persistence of such pollutants in aquatic environments, albeit at low concentrations, presents serious ecotoxicological risks, with possibilities of disrupting aquatic life and human health through bioaccumulation and water-based exposure pathways (Mohammadhosseini et al., 2022). Rhodamine B (Rh B) is highly water-soluble xanthene dye that exists in two structurally pH-dependent forms: a fluorescent open form that dominates under acid conditions, and a non-fluorescent spirolactam (closed form) that predominates in alkaline media. Rh B is environmentally persistent and resists microbial degradation, and thereby poses significant aquatic pollution. Even at trace concentrations, it can exert extreme toxicological effects on aquatic organisms, including respiratory and reproductive toxicity, tissue necrosis, and carcinogenesis. In humans, chronic exposure has been linked to mutagenic effects. Because of its toxicity and stability, it is of paramount interest to come up with better remediation technologies for Rh B-contaminated wastewaters to protect aquatic life and public health (Bashofi & Prasetyo, 2023)

The methods for treating dye-containing wastewater are generally categorized into physical processes (e.g., adsorption, ion exchange, coagulation-flocculation, membrane filtration), chemical processes (e.g., oxidation, electrochemical processes, Fenton reaction), and biological processes (e.g., natural attenuation, bioaugmentation, biostimulation, bioleaching, rhizoremediation) (Ahmad et al., 2021). Adsorption has emerged as a highly efficient and cost-effective technique for removing dyes, pigments, phenolic compounds, and other chemical contaminants from wastewater. Its effectiveness in treating high-concentration dye solutions, combined with low operational costs and simple system design, makes it an attractive option for industrial wastewater treatment. Various adsorbent materials have been developed for dye remediation, including bentonite clay, peanut husk biomass, polydopamine-based microspheres, and tin oxide ($SnO_2$) nanoparticles (Al-Kazragi & Al-Heetimi, 2021). Bentonite, composed of aluminum silicate minerals, has become a major focus in dye removal due to its uniform porosity, wide interlayer spacing, and non-swelling behavior (Li et al., 2024). Because of its inertness, thermal stability, and eco-friendliness, bentonite is suitable for use in catalytic processes. Its activity is often enhanced through functionalization with metals or metal oxides, where $Na^+$ ions have been shown to increase surface area and basal spacing (Chauhdary et al., 2022). According to (Warsono et al., 2018), Indonesian natural bentonite modified through pillaring with Al, Cu, Mn, and Ti exhibited enhanced dye removal capability: the cation exchange capacity (CEC) increased up to 125.3 meq/100 g in the HTiB modification compared to 98 meq/100 g in the raw bentonite, and the specific surface area (SSA) rose to 151.3 $m^2/g$ in the HAlB modification compared to approximately 70.7 $m^2/g$ in the raw bentonite. Nano-silica has emerged as one of the materials with high pozzolanic reactivity, good thermal stability, and compatibility with cementitious systems.

The particle size of nano-silica is smaller than that of ordinary cement particles, allowing for better dispersion, higher surface area, and stronger interactions with other

components in composite matrices. These properties make nano-silica highly beneficial not only for improving the mechanical strength and durability of construction materials but also for facilitating adsorption and catalytic reactions in environmental remediation processes (Singh et al., 2020). The bentonite–nano silica composite is expected to enhance adsorption performance through increased surface reactivity, additional active sites, and improved pore structure. In this study, the adsorption performance of the bentonite–nano $SiO_2$ composite will be evaluated for the decolorization of Rhodamine B from wastewater. The research focuses on the effect of bentonite modified with silica on dye decolorization efficiency.

## 2. MATERIALS AND METHODS

### *2.1. Materials*

The materials employed in this study included bleaching earth (BE) of the bentonite type (Indonesian brand), nano $SiO_2$ (Merck), Rhodamine B (Merck) as a model dye for wastewater simulation, and 95% ethanol (Merck) used as a solvent for the modification process.

### *2.2. Methods*

This research was carried out in two main stages. The first stage was the preparation of the bentonite–nano $SiO_2$ composite material, and the second stage was the adsorption process, in which the prepared composite was used for the decolorization of Rhodamine B dye solution.

### *2.3. Preparation of BE-nano $SiO_2$*

To prepare the BE–nano $SiO_2$ composite, 50 g of BE was blended with nano-$SiO_2$ at a concentration of 15% (w/w of BE) using 50 mL of 95% ethanol as the solvent. The mixture was continuously stirred for 3 hours at 70 °C to facilitate the modification process. The resulting BE–$SiO_2$ composite was then filtered and dried in an oven at 100 °C for 5 hours (Yahya et al., 2024).

The modified bentonite was subsequently characterized using SEM and FTIR analyses. The surface morphology of the bentonite–nano $SiO_2$ composite was examined using a scanning electron microscope (JSM-6510LV, JEOL Ltd., Tokyo, Japan) operated at 20 kV under a magnification of 3000×. Meanwhile, the crystallinity of the particles was analyzed using an X-ray diffractometer (MAXima_X XRD-7000, Shimadzu, Japan). Furthermore, the functional groups of the material were identified using Fourier Transform Infrared (FTIR) spectroscopy (PerkinElmer Spotlight 200, PerkinElmer Inc., Waltham, MA, USA).

### *2.4. Adsorption Process*

The adsorption process was carried out by preparing a 1 ppm Rhodamine B solution as a simulated dye wastewater. Adsorption was then conducted using various concentrations of bentonite–nano $SiO_2$ adsorbent (0.10%, 0.25%, 0.50%, 0.75%, and 1% w/v) to determine the effect of adsorbent concentration on decolorization performance. The adsorption process was performed under continuous stirring for 30 minutes, after which the mixture was separated by centrifugation.

The optimum adsorbent concentration obtained from this stage was subsequently used to investigate the effect of contact time on adsorption efficiency, with contact times of 5, 10, 15, and 30 minutes. The residual concentration of Rhodamine B after adsorption was measured using a UV-Vis spectrophotometer.

## 3. RESULTS AND DISCUSSION

### *3.1. Performance Evaluation of Bentonite–Nano $SiO_2$ in Rhodamine B Adsorption*

The adsorption performance of Bentonite–Nano $SiO_2$ in removing Rhodamine B dye was investigated by analyzing two major factors: adsorbent concentration and adsorption time.

Adsorption is a surface phenomenon influenced by both the amount of adsorbent available and the contact duration between the adsorbent and adsorbate (Huda et al., 2025). Rhodamine B, being a cationic dye, tends to interact electrostatically with negatively charged surfaces, such as those present in bentonite-based composites. The modification of bentonite with nano-silica is expected to enhance its surface area and improve its adsorption efficiency due to increased active sites and surface reactivity.

*3.1.1. Effect of Adsorbent Concentration*

The performance evaluation of bentonite–nano $SiO_2$ with varying adsorbent concentrations was carried out to determine the effect of nano $SiO_2$ addition on the adsorption capability of bentonite in the bleaching process. The variation in concentration aimed to identify the optimum composition that provides the highest adsorption efficiency for the decolorization of Rhodamine B. The performance results of bentonite–nano $SiO_2$ with different concentrations are presented in **Figure 1**. Figure 1 shows the effect of Bentonite–Nano $SiO_2$ adsorbent concentration on the residual Rhodamine B concentration and adsorption percentage. At an adsorbent concentration of 0.1% (w/v), Bentonite–Nano $SiO_2$ reduced the Rhodamine B concentration from 1 ppm to 0.177 ppm, with an adsorption percentage of 82.29%. Increasing the adsorbent concentration to 0.75% (w/v) further decreased the Rhodamine B concentration to 0.11 ppm, while a higher concentration of 1.0% (w/v) resulted in only a small additional reduction, reaching 0.09 ppm. These results indicate that at higher adsorbent concentrations, the adsorption efficiency tends to approach saturation because most dye molecules have already been adsorbed (Legarto et al., 2019). This observation is consistent with the study by (Eleraky, 2022), which reported that increasing the bentonite dosage in methylene blue adsorption enhanced dye removal efficiency until a stable level was reached. Therefore, an adsorbent concentration of 0.75% (w/v) can be considered the optimum condition, achieving an adsorption percentage of 88.98%.

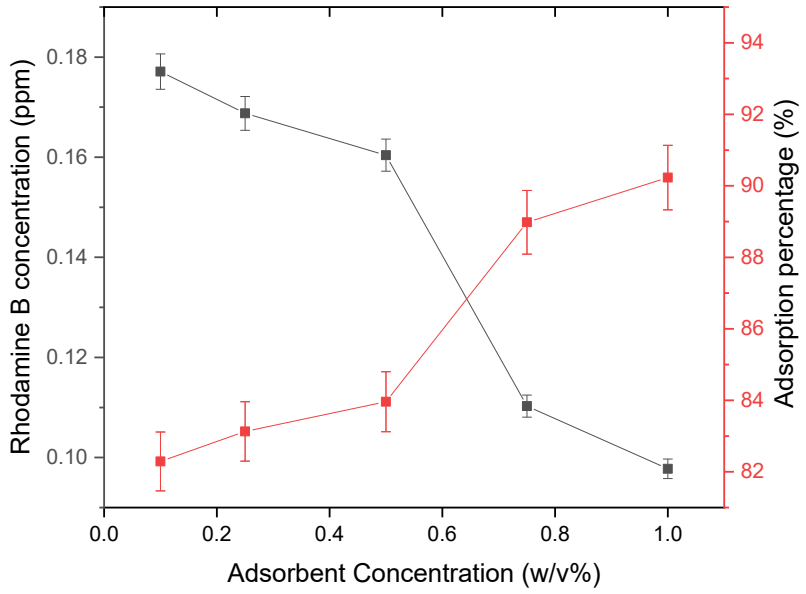


**Figure 1.** Evaluation of Bentonite–Nano $SiO_2$ Performance at Different Concentrations

### *3.1.2. Effect of Adsorption Time*

The duration of contact between the adsorbent and dye molecules plays a crucial role in determining adsorption efficiency, as it governs the extent of interaction between the dye and the active sites on the adsorbent surface (Haleem et al., 2023). The effect of contact time on the adsorption process can be observed in **Figure 2**.

**Figure 2** shows the effect of contact time on the adsorption of Rhodamine B. The residual Rhodamine B concentration decreased significantly during the first 10–15 minutes, indicating that most of the adsorption occurred at the initial stage. At this stage, the adsorption percentage reached approximately 90%, with a residual Rhodamine B concentration of 0.099 ppm, which suggests a rapid interaction between dye molecules and the active sites on the adsorbent surface. After this period, the adsorption process became stable up to 30 minutes, as indicated by only a slight change in the residual Rhodamine B concentration. This behavior indicates that most of the available active sites had been occupied and the system was approaching adsorption equilibrium. A similar trend has been reported in studies using bentonite or kaolin–bentonite composites, where the adsorption rate increased sharply in the early minutes and then remained nearly constant, confirming that equilibrium had been reached (He et al., 2022).

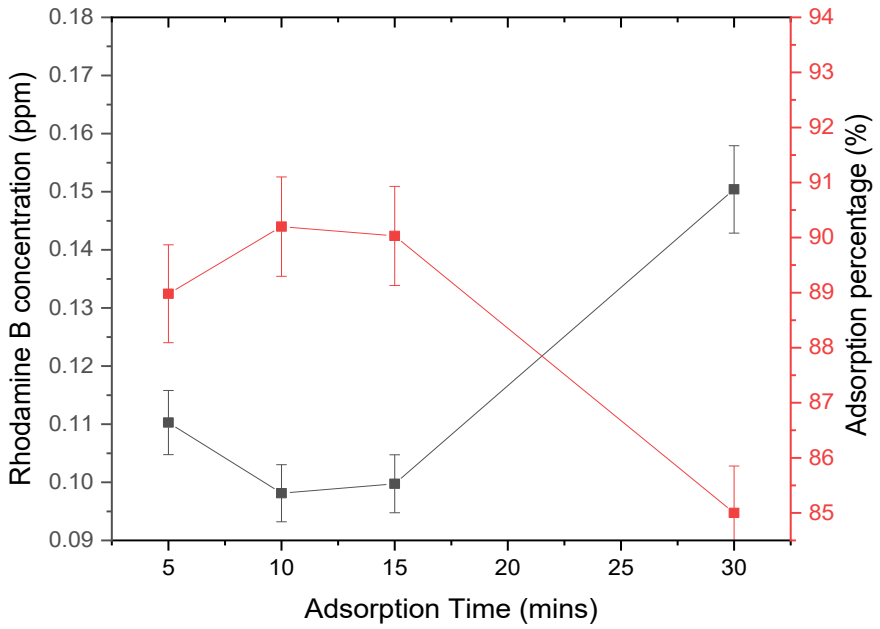


**Figure 2.** Evaluation of Adsorption Time

### *3.1.3. Bentonite–Nano $SiO_2$ Characterization*

Characterization of the Bentonite–Nano $SiO_2$ composite was conducted using Scanning Electron Microscopy (SEM) and Fourier Transform Infrared Spectroscopy (FTIR) to understand its morphological and structural changes after modification. SEM provides insight into the surface morphology and particle distribution, while FTIR identifies functional groups and chemical bonds present in the material. Comparing unmodified bentonite with Bentonite–Nano $SiO_2$ helps

determine the success of the modification process and the interaction between silica nanoparticles and bentonite layers (Pereira et al., 2015). The results of the characterization using SEM can be seen in **Figure 3**.

**Figure 3** presents the surface morphology analysis obtained using Scanning Electron Microscopy (SEM), which reveals distinct differences between unmodified bentonite and the Bentonite–Nano $SiO_2$ composite. The unmodified bentonite (Figure A) exhibits relatively compact and irregularly shaped particles with visible agglomeration among particles. This morphological characteristic indicates low porosity and a limited number of active sites on the surface, which can directly reduce the adsorption efficiency toward dye molecules (Frida et al., 2022). In contrast, the Bentonite–Nano $SiO_2$ composite (Figure B) shows a rougher surface texture with more numerous and uniformly distributed pores. This observation suggests that the nano-silica particles were successfully dispersed and firmly attached to the bentonite layers. The incorporation of nanosized silica into the bentonite structure is known to promote interlayer intercalation and basal spacing expansion, resulting in an increased specific surface area and a greater number of active sites for adsorption (Rind et al., 2023).

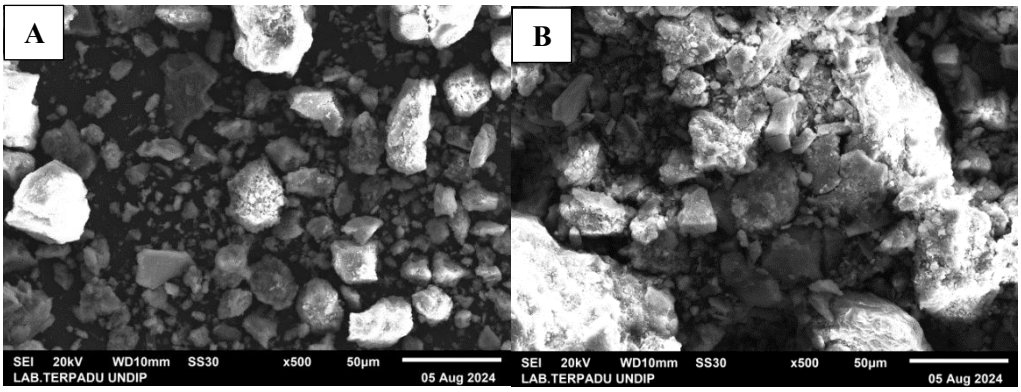


**Figure 3.** SEM Results A) Unmodified Bentonite and B) Bentonite–Nano $SiO_2$ Composite

These findings demonstrate that nano-silica particles function as structural reinforcements that prevent bentonite particle agglomeration, maintain dispersion stability, and strengthen interlayer bonding through Si–O–Si and Si–O–Al interactions (Gustave et al., 2022). This result is consistent with the study by Suzuki et al. (2024), who reported that bentonite modified with nano-silica exhibited a more open porous morphology and an enhanced adsorption capacity for methylene blue dye, achieving up to an 85% improvement compared to raw bentonite (Suzuki, 2024). FTIR spectra further confirm the successful modification of bentonite with nano-silica. Both samples show characteristic absorption peaks around 1000–1100 $cm^{-1}$, corresponding to Si–O–Si stretching vibrations typical of silicate structures. However, the intensity of this peak increases in Bentonite–Nano $SiO_2$, indicating the incorporation of additional Si–O bonds from nano-silica. The broad band near 3400 $cm^{-1}$ corresponds to O–H stretching vibrations from hydroxyl groups and interlayer water, while the peak around 1630 $cm^{-1}$ represents the bending of adsorbed water molecules. The presence of these peaks in both materials confirms that the bentonite structure is maintained after modification, but the increased Si–O–Si signal demonstrates the chemical interaction between bentonite and nano-silica (Perez et al., 2022).

The combination of SEM and FTIR analyses confirms that the modification process effectively enhances the physicochemical properties of bentonite. The addition of nano-silica increases surface roughness and porosity, while strengthening the silicate framework through additional Si–O–Si bonds. These structural improvements contribute to better adsorption performance by providing more active sites and stronger surface interactions with adsorbates such as Rhodamine B. Therefore, Bentonite–Nano $SiO_2$ can be considered a promising adsorbent material for wastewater treatment applications due to its enhanced surface characteristics and chemical stability (Suzuki, 2024).

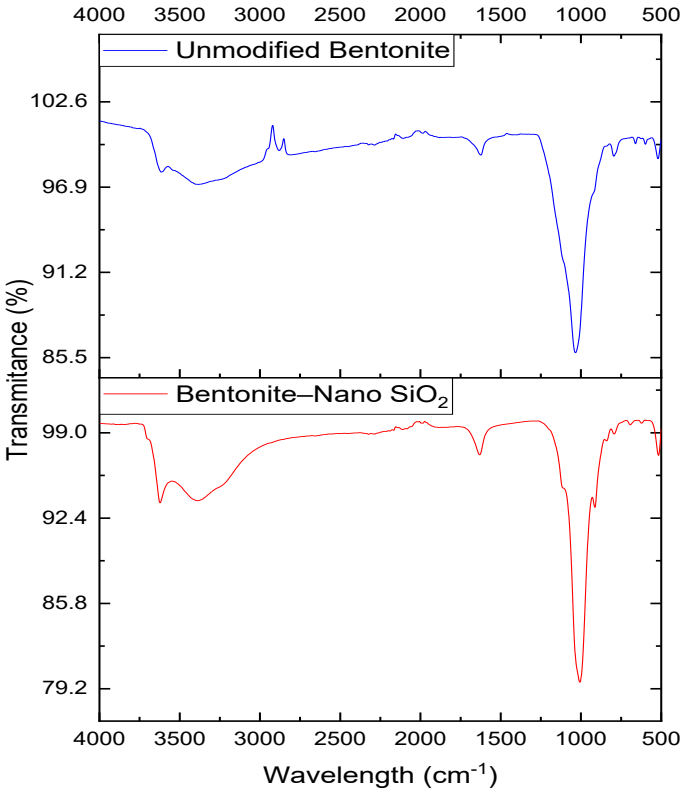


**Figure 4.** FTIR Spectra of Unmodified Bentonite and Bentonite–Nano $SiO_2$ Composite

## 4. CONCLUSIONS

he modification of bentonite with nano-silica ($SiO_2$) effectively enhanced its adsorption capacity and surface properties. The optimal adsorption of Rhodamine B was achieved at a concentration of 0.75% (w/v) and a contact time of 10–15 minutes, with an efficiency of about 90%. SEM and FTIR analyses confirmed successful modification, showing increased surface roughness, porosity, and the formation of additional Si–O–Si bonds. These improvements provide more active sites and stronger interactions with dye molecules. Therefore, Bentonite–Nano $SiO_2$ demonstrates strong potential as an efficient and eco-friendly adsorbent for wastewater treatment applications.

## ACKNOWLEDGMENT

We would like to express our gratitude to the team and all parties involved, especially the laboratory of Politeknik ATI Padang. May

we continue to stay motivated and produce even better research in the future.

## LIST OF REFERENCES

Ahmad, W. S., Nur, A. Y., & Albakar, F. A. (2021). Biodegradation of Textile Dye Rhodamine B by Biofilm-Forming Bacteria. ALCHEMY Jurnal Penelitian Kimia, 17(2), 151–158. https://doi.org/10.20961/alchemy.17.2.49010.151-158

Al-Kazragi, M. A. U. R., & Al-Heetimi, D. T. A. (2021). Removal of toxic dye (Rhodamine B) from aqueous solutions by natural smectite (SMC) and SMC-nanoTiO2. Desalination and Water Treatment, 230. https://doi.org/10.5004/dwt.2021.27403

Bashofi, S. A. R., & Prasetyo, A. (2023). Degradation of Rhodamine B by $Bi_4Ti_3O_{12}$ Obtained via the NaCl/KCl Mixed Molten Salt Method. POSITRON, 13(2). https://doi.org/10.26418/positron.v13i2.69085

Chauhdary, Y., Hanif, M. A., Rashid, U., Bhatti, I. A., Anwar, H., Jamil, Y., Alharthi, F. A., & Kazerooni, E. A. (2022). Effective Removal of Reactive and Direct Dyes from Colored Wastewater Using Low-Cost Novel Bentonite Nanocomposites. Water (Switzerland), 14(22). https://doi.org/10.3390/w14223604

Eleraky, M. (2022). Removal Of Methylene Blue Dye By Activated Egyptian Bentonite Clay. Journal of Environmental Science, 0(0). https://doi.org/10.21608/jes.2022.148634.1278

Frida, E., Bukit, N., Astianta Bukit, F. R., & Bukit, B. F. (2022). Analysis Structure and Morphology of Bentonite-Opba Nanocomposites as Nanofillers. Journal of Applied Research and Technology, 20(2). https://doi.org/10.22201/icat.24486736e.2022.20.2.1710

Gustave, T., Chantale Njiomou, D., Charles Fon, A., Danie Laure Mbella, M., Guillonnel Trésor Nyadjou, D., Jean Marie, K., & Philippe, B. (2022). Nano-silica from kaolinitic clay used as adsorbent for anionic and cationic dyes removal: linear and non-linear regression isotherms and kinetics studies. Annals of Civil and Environmental Engineering, 6(1). https://doi.org/10.29328/journal.acee.1001034

Haleem, A., Shafiq, A., Chen, S. Q., & Nazar, M. (2023). A Comprehensive Review on Adsorption, Photocatalytic and Chemical Degradation of Dyes and Nitro-Compounds over Different Kinds of Porous and Composite Materials. In Molecules (Vol. 28, Issue 3). https://doi.org/10.3390/molecules28031081

He, H., Chai, K., Wu, T., Qiu, Z., Wang, S., & Hong, J. (2022). Adsorption of Rhodamine B from Simulated Waste Water onto Kaolin-Bentonite Composites. Materials, 15(12). https://doi.org/10.3390/ma15124058

Huda, M. F. F., Mustopa, Aktawan, A., & Hakika, D. C. (2025). Metal Adsorption in Batik Liquid Waste Using Adsorbents from Duck Eggshell and Durian Skin Waste. Indonesian Journal of Chemical Engineering, 3(1), 10–16. https://doi.org/10.26555/ijce.v3i1.1419

Kolya, H., & Kang, C. W. (2024). Toxicity of Metal Oxides, Dyes, and Dissolved Organic Matter in Water: Implications for the Environment and Human Health. In

Toxics (Vol. 12, Issue 2). https://doi.org/10.3390/toxics12020111

Li, Z., Cheng, F., Li, Y., Wu, D., Yang, D., Sun, D., Cheng, D., & Tian, W. (2024). Bentonite-assisted construction of magnesium-silicate-based composite as efficient adsorbent for organic dye removal. Journal of Experimental Nanoscience, 19(1). https://doi.org/10.1080/17458080.2023.2292230

Małachowska, E., Dubowik, M., Boruszewski, P., & Przybysz, P. (2021). Accelerated ageing of paper: effect of lignin content and humidity on tensile properties. Heritage Science, 9(1). https://doi.org/10.1186/s40494-021-00611-3

Mohammadhosseini, S., Al-Musawi, T. J., Romero Parra, R. M., Qutob, M., Gatea, M. A., Ganji, F., & Balarak, D. (2022). UV and Visible Light Induced Photodegradation of Reactive Red 198 Dye and Textile Factory Wastewater on Fe2O3/Bentonite/TiO2 Nanocomposite. Minerals, 12(11). https://doi.org/10.3390/min12111417

Nabizadeh, R., Amrollahi, R., Ghafary, B., & Norouzian Alam, S. (2023). Influence of ozone supply mode and aeration on photocatalytic ozonation of organic pollutants in wastewater using TiO2 and ZnO nanoparticles. Heliyon, 9(12). https://doi.org/10.1016/j.heliyon.2023.e22854

Pereira, D. S., Lisboa, V. N. F., Silva, I. A., Figueirêdo, J. M. R., Neves, A., & Menezes, R. R. (2015). Bentonite clays characterization in the town of sossego – Paraiba state. Materials Science Forum, 820. https://doi.org/10.4028/www.scientific.net/MSF.820.65

Perez, F. M., Santori, G. F., Pompeo, F., & Nichio, N. N. (2022). Silica-Resin-Bentonite Nanocomposite and Its Application in Catalysis. Minerals, 12(12). https://doi.org/10.3390/min12121486

Rind, I. K., Sarı, A., Tuzen, M., Lanjwani, M. F., & Saleh, T. A. (2023). Synthesis of bentonite/SiO2/magnetite nanostructure as an efficient adsorbent for Bisphenol A removal from waters. Industrial Crops and Products, 201. https://doi.org/10.1016/j.indcrop.2023.116905

Singh, B., Na, J., Konarova, M., Wakihara, T., Yamauchi, Y., Salomon, C., & Gawande, M. B. (2020). Functional mesoporous silica nanomaterials for catalysis and environmental applications. In Bulletin of the Chemical Society of Japan (Vol. 93, Issue 12). https://doi.org/10.1246/BCSJ.20200136

Suzuki, R. (2024). Effect of Adding Bentonite to Porous Silica via the Sol-Gel Method. ACS Omega, 9(9), 10577–10582. https://doi.org/10.1021/acsomega.3c08832

Warsono, H. R. S., Kurniawan, W., & Hinode, H. (2018). Utilization of modified indonesia natural bentonite for dye removal. ASEAN Journal of Chemical Engineering, 18(2).

Yahya, A. K., Nurmalasari, E., Aini, A. P., & Ulya, H. N. (2024). Performance Evaluation of Bentonite/Nano-SiO2 Composite as Bleaching Earth in Crude Palm Oil Processing. Jurnal Kimia Sains Dan Aplikasi, 27(4), 167–173. https://doi.org/10.14710/jksa.27.4.167-173

**Jurnal Ilmiah Berkala: Sains dan Terapan Kimia**
*Vol. 20 No. 1, January 2026*

# Efficiency of Chitosan and Alum as Coagulants for Peat Water Treatment

# Efisiensi Kitosan Dan Tawas Sebagai Koagulan Untuk Pengolahan Air Gambut

**Utami Irawati*, Dahlena Ariyani, Taufiqur Rohman**

[1]Departement of Chemistry, Faculty of Mathematics and Natural Sciences, Universitas Lambung Mangkurat, Jl. A. Yani Km 36, Banjarbaru 70714, Indonesia

*Email: uirawati@ulm.ac.id

## ABSTRACT

*Peat water is widely found in swamp and lowland areas of Indonesia and is characterized by high color intensity, low pH, and elevated concentrations of dissolved organic compounds. These characteristics limit its direct use as a water source and require appropriate treatment methods. This study evaluates the effectiveness of chitosan and alum as coagulants in improving the quality of peat water. The optimum dosage and pH conditions for the coagulation process were determined based on reductions in turbidity and organic compound levels after treatment. The results indicate that the optimum dosage for chitosan was 5 mg/L, while alum required 15 mg/L to achieve effective turbidity removal. Under these conditions, turbidity reductions of 81.91% and 76.28% were obtained for chitosan and alum, respectively. The coagulation performance of both coagulants was strongly influenced by pH. Chitosan showed optimum performance at pH 8, resulting in a turbidity reduction of 83.36%, whereas alum exhibited the best performance at pH 7, achieving a turbidity reduction of 88.02%. Further analysis revealed that alum was more effective than chitosan in reducing the concentration of organic compounds in peat water. Overall, the findings demonstrate that both coagulants can improve peat water quality, although their performance varies depending on operational conditions such as dosage and pH.*

**Keywords:** Peat water, chitosan, alum, coagulation, flocculation.

**Received**: 09 March 2026; **Accepted**: 12 March 2026 : **Available online**: 12 March 2026

## 1. INTRODUCTION

Peat water is a type of surface water commonly found in swamp areas, coastal regions, and lowland environments, particularly in peatland ecosystems across Sumatra and Kalimantan. This type of water typically exhibits a dark brown to reddish color caused by the presence of dissolved humic substances (Kusnadi, 2010). The high concentration of humic acids and other dissolved organic compounds results in several characteristic properties of peat water, including high organic content, low pH, unpleasant odor, and intense coloration. These characteristics significantly reduce its suitability for direct consumption and may lead to potential health risks if consumed over a long period.

Due to these limitations, various studies have investigated methods to improve peat water quality so that it can be used as a reliable water source. One such study conducted by Rehansyah et al. (2017) reported that appropriate treatment processes are capable of reducing organic substances and color in peat water, thereby improving its suitability as raw water. Among the various treatment technologies available, coagulation is widely applied as an effective method to reduce turbidity and remove suspended particles from water. Research on water clarification through coagulation processes has been extensively conducted. Various types of coagulants have been tested for their effectiveness in improving water quality, including both synthetic and natural coagulants. Synthetic coagulants are commonly used in water treatment processes because they are relatively easy to obtain and economically feasible. However, excessive use of synthetic coagulants may cause environmental and health concerns since many of these materials are not readily biodegradable (Sunardi et al., 2013).

Therefore, there is growing interest in exploring natural materials as alternative coagulants for peat water treatment. One potential natural coagulant is chitosan, a biopolymer derived from chitin (Hendrawati et al., 2015). Chitosan has been widely studied due to its biodegradable nature, non-toxic properties, and strong ability to interact with suspended particles in aqueous systems.

Previous research by Mu'minah (2008) demonstrated that chitosan can function as an effective and efficient coagulant compared with alum, as evidenced by the reduction of water turbidity even at relatively low concentrations of chitosan. Furthermore, Amir and Isnaniawardhana (2010) reported that the efficiency of color removal in water treatment is largely determined by the collision frequency between destabilized colloidal particles, which subsequently form larger flocs that can settle more easily.

Based on these considerations, this study aims to evaluate the efficiency of chitosan and alum as coagulants for peat water treatment. Specifically, the study examines the influence of coagulant dosage and pH on the reduction of turbidity and organic compounds in peat water. In addition, the optimal dosage and pH conditions for the coagulation process are determined in order to obtain the most effective formulation for the application of chitosan and alum as coagulants in peat water treatment.

## 2. MATERIALS AND METHODS

### *2.1. Instruments and Materials*

The instruments used in this study included standard laboratory glassware, a magnetic stirrer, thermometer, jar test apparatus (VELP Scientifica JLT-6), pH meter (HACH sensION+ PH1), analytical balance (Ohaus PA224), hot plate, turbidimeter (HACH Model 2100Q), sample bottles, volumetric flasks, and plastic containers for water sampling. The materials used consisted of peat water samples, chitosan (degree of deacetylation 87.5%), alum ($Al_2(SO_4)_3$), acetic acid ($CH_3COOH$, p.a., Merck), sodium hydroxide (NaOH, p.a., Merck), hydrochloric acid (HCl, p.a., Merck), sulfuric acid ($H_2SO_4$, p.a., Merck), oxalic acid ($H_2C_2O_4$, p.a., Merck), potassium permanganate ($KMnO_4$, p.a., Merck), and distilled water.

### *2.2. Methods*

This study was conducted to evaluate the efficiency of chitosan and alum as coagulants for peat water treatment. The experimental procedures consisted of several stages, including the preparation of coagulant solutions, determination of optimum coagulant dosage, determination of optimum

pH conditions, and evaluation of coagulant efficiency in reducing turbidity and organic compounds in peat water. The organic matter content in the treated water was determined using the permanganometric method according to the Indonesian National Standard (SNI 06-6989.22-2004).

The overall experimental workflow involved coagulation–flocculation tests using a jar test apparatus, followed by turbidity measurement and analysis of organic matter concentration. The detailed procedures for each stage are described in the following sections.

*2.2.1 Preparation of Coagulant Solutions*

The preparation of the chitosan solution followed the method suggested by Pontius et al. (2016). Chitosan (20 g) was dissolved in 1000 mL of 2% acetic acid solution to obtain a 2% (w/v) chitosan solution. The mixture was continuously stirred for approximately one hour until a homogeneous solution was obtained. A similar preparation procedure was applied for the alum coagulant solution.

*2.2.2 Determination of Optimum Coagulant Dosage and pH*

The determination of optimum dosage and pH conditions was carried out using a jar test coagulation process. A total of 1000 mL of peat water sample was placed in the jar test apparatus. The coagulant dosage was varied at 5, 10, 15, 20, and 25 mg/L, while the pH was adjusted within the range of pH 5–9. The coagulation process consisted of rapid mixing at 100 rpm for 1 minute, followed by slow mixing at 45 rpm for 20 minutes. After mixing, the suspension was allowed to settle for 30 minutes to facilitate sedimentation. The turbidity of the treated water was then measured using a turbidimeter.

*2.2.3 Determination of Coagulant Efficiency*

The efficiency of each coagulant was evaluated using the optimum dosage and pH conditions obtained from the previous experiments. A total of 500 mL of peat water was placed in a beaker and treated with the respective coagulant. The coagulation process was conducted using the same jar test procedure: rapid mixing at 100 rpm for 1 minute, followed by slow mixing at 45 rpm for 20 minutes. The treated samples were then allowed to settle for 30 minutes, after which the turbidity of the supernatant was measured.

*2.2.4 Determination of Organic Matter Content by Permanganometric Method*

The determination of organic matter content in peat water was performed using the permanganometric method according to the Indonesian National Standard SNI 06-6989.22-2004. A volume of 100 mL of peat water sample (before and after treatment) was transferred into an Erlenmeyer flask, and several boiling chips were added. The sample was then treated with a few drops of 0.01 N $KMnO_4$ solution until a faint pink color appeared. Subsequently, 5 mL of 8 N $H_2SO_4$ was added to the solution.

The mixture was heated to approximately 105 °C, followed by the addition of 10 mL of 0.01 N $KMnO_4$ standard solution. The sample was boiled for 10 minutes, after which 10 mL of 0.01 N oxalic acid ($H_2C_2O_4$) was added. The solution was then titrated with 0.01 N $KMnO_4$ until a persistent pale pink endpoint was observed. The volume of $KMnO_4$ required to reach the titration endpoint was recorded and used to determine the permanganate value, which represents the concentration of organic compounds present in the peat water sample.

## 3. RESULTS AND DISCUSSION

*3.1 Determination of Optimum Coagulant Dosage*

Coagulant dosage is a critical parameter influencing the efficiency of the coagulation–flocculation process. Both insufficient and excessive dosages may reduce the effectiveness of particle destabilization and

floc formation. Insufficient coagulant results in incomplete neutralization of suspended particles, while excessive dosage may lead to particle restabilization (Rao, 2015).

The effect of coagulant dosage on turbidity removal from peat water is presented in **Table 1**. In this study, the dosage of both chitosan and alum was varied from 5 to 25 mg/L.

**Table 1.** Effect of coagulant dosage on turbidity removal from peat water

| Dosage (mg/L) | Chitosan Final Turbidity (NTU) | Removal (%) | Alum Final Turbidity (NTU) | Removal (%) |
|---|---|---|---|---|
| 5 | 0.74 | 81.91 | 4.01 | 1.96 |
| 10 | 4.38 | -7.09 | 1.36 | 66.75 |
| 15 | 4.48 | -9.54 | 0.97 | 76.28 |
| 20 | 4.37 | -6.85 | 1.31 | 67.97 |
| 25 | 4.63 | -13.20 | 1.01 | 75.31 |

Note: Initial turbidity ($T_0$) = 4.09 NTU. According to SNI 01-3553-2006, the maximum turbidity level for raw water is 5 NTU

As shown in Table 1, the addition of chitosan significantly reduced the turbidity of peat water at low dosage. The optimum dosage for chitosan was observed at 5 mg/L, resulting in a final turbidity of 0.74 NTU, corresponding to a turbidity removal efficiency of 81.91%. This turbidity value meets the Indonesian raw water quality standard, which specifies a maximum turbidity limit of 5 NTU (SNI 01-3553-2006).

However, increasing the dosage of chitosan beyond this concentration did not improve turbidity removal. At higher dosages (10–25 mg/L), the turbidity values increased to 4.38–4.63 NTU, and the calculated removal efficiency even became negative. This phenomenon may occur due to overdosing of the polymer coagulant, which can lead to the restabilization of suspended particles when excess polymer chains remain in the solution.

Compared with chitosan, alum required a higher dosage to achieve effective turbidity removal. The optimum dosage for alum was 15 mg/L, which produced a final turbidity of 0.97 NTU and a removal efficiency of 76.28%. The coagulation mechanism of alum involves the release of $Al^{3+}$ ions in aqueous solution.

These positively charged ions neutralize negatively charged colloidal particles suspended in water, enabling them to aggregate and form larger flocs that can settle more easily. The higher dosage required for alum may be associated with the characteristics of suspended particles in peat water, which are dominated by macromolecular humic substances. These particles generally require a higher concentration of metal ions to effectively neutralize their surface charge before aggregation occurs.

Chitosan, on the other hand, contains amino functional groups (–$NH_2$) that can be protonated to form –$NH_3^+$ groups in aqueous media. These positively charged sites interact electrostatically with negatively charged colloidal particles, promoting particle destabilization and floc formation. According to Agusnar (2003), the coagulation mechanism of chitosan commonly occurs through adsorption and interparticle bridging, where polymer chains act as bridges that connect multiple particles and form larger flocs.

Overall, the results indicate that chitosan is more efficient than alum in terms of the dosage required to achieve optimal turbidity removal, although alum still provides effective turbidity reduction under appropriate conditions.

*3.2 Determination of Optimum pH*

The pH of the solution plays an important role in the coagulation–flocculation process because it influences the surface charge of suspended particles as well as the chemical speciation of the coagulant. Changes in pH can therefore significantly affect the efficiency of particle destabilization and floc formation. Previous studies have reported that the effectiveness of coagulation processes strongly depends on the pH conditions of the treated water (Herawati et al., 2017).

The effect of pH on turbidity removal using chitosan and alum is presented in **Table 2**. For chitosan, turbidity removal increased significantly as the pH approached neutral and slightly alkaline conditions.

**Table 2.** Effect of pH on turbidity removal using chitosan and alum

| pH | Chitosan Final Turbidity (NTU) | Removal (%) | Alum Final Turbidity (NTU) | Removal (%) |
|---|---|---|---|---|
| 5 | 11.7 | 12.69 | 3.07 | 74.63 |
| 6 | 11.4 | 14.93 | 1.78 | 85.29 |
| 7 | 3.22 | 75.97 | 1.45 | 88.02 |
| 8 | 2.23 | 83.36 | 2.45 | 79.75 |
| 9 | 3.04 | 77.31 | 2.27 | 81.24 |

Note: Initial turbidity = 13.4 NTU (chitosan) and 12.1 NTU (alum). According to SNI 01-3553-2006, the maximum turbidity standard for raw water is 5 NTU.

As shown in Table 2, the highest turbidity removal was obtained at pH 8, where the final turbidity decreased to 2.23 NTU, corresponding to a removal efficiency of 83.36%. At lower pH values (pH 5–6), the turbidity removal efficiency was much lower, with reductions of only 12.69% and 14.93%, respectively.

This behavior is closely related to the chemical characteristics of humic substances present in peat water. Under acidic conditions, many functional groups within humic substances remain protonated, resulting in fewer negatively charged sites available for electrostatic interaction with the coagulant. As a result, the interaction between humic particles and chitosan becomes weaker, leading to lower coagulation efficiency.

At near-neutral and slightly alkaline pH values, humic substances contain a greater number of deprotonated carboxylate groups (–$COO^-$). These negatively charged groups can interact electrostatically with the protonated amino groups (–$NH_3^+$) present in chitosan molecules. This interaction promotes particle destabilization and facilitates the formation of larger flocs that settle more easily. In contrast, the optimum coagulation performance for alum was observed at pH 7, where turbidity decreased to 1.45 NTU, corresponding to a

removal efficiency of 88.02%, as shown in Table 2. Alum also exhibited relatively good turbidity removal across the investigated pH range, although the highest efficiency was achieved near neutral conditions.

According to Hu et al. (2006), aluminum-based coagulants generally perform best within a limited pH range and may lose efficiency under strongly acidic or highly alkaline conditions. At low pH values, aluminum tends to exist predominantly as monomeric $Al^{3+}$ species, which are less effective in destabilizing suspended particles. When alum is dissolved in water, it undergoes hydrolysis to form various aluminum hydroxo complexes, and the distribution of these species strongly depends on the pH of the solution (Yang et al., 2010).

These hydrolysis products eventually form amorphous $Al(OH)_3$ precipitates, which act as sweep flocs capable of adsorbing suspended particles and organic substances from the water. This mechanism explains why alum shows high turbidity removal efficiency at pH values close to neutral. Overall, the results indicate that both coagulants are influenced by pH conditions. Chitosan exhibited optimum performance at pH 8, while alum achieved its highest efficiency at pH 7. These findings highlight the importance of controlling pH conditions in order to optimize the coagulation process for peat water treatment.

*3.3 Evaluation of Coagulant Efficiency*

The coagulation efficiency of chitosan and alum under their respective optimum conditions was further evaluated using three different peat water samples. The results of turbidity reduction obtained using both coagulants are summarized in **Table 3**.For sample 1, the initial turbidity of the peat water was 14.1 NTU. After treatment with chitosan, the turbidity decreased to 2.32 NTU, corresponding to a turbidity removal efficiency of 83.58%.

**Table 3.** Comparison of turbidity removal efficiency of chitosan and alum

| Sample | Treatment | Turbidity (NTU) | Turbidity Reduction (NTU) | Removal (%) |
|---|---|---|---|---|
| 1 | Control | 14.1 | 0 | 0 |
| | Chitosan | 2.32 | 11.79 | 83.58 |
| | Alum | 1.88 | 12.23 | 86.70 |
| 2 | Control | 14.1 | 0 | 0 |
| | Chitosan | 2.58 | 11.52 | 81.70 |
| | Alum | 2.29 | 11.82 | 83.79 |
| 3 | Control | 1.34 | 0 | 0 |
| | Chitosan | 1.55 | -0.21 | -15.30 |
| | Alum | 0.77 | 0.57 | 42.54 |

When alum was used as the coagulant, the turbidity decreased further to 1.88 NTU, resulting in a removal efficiency of 86.70%. These results indicate that both coagulants were highly effective in reducing turbidity under these conditions. A similar trend was observed for sample 2, where the initial turbidity was also 14.1 NTU. Treatment with chitosan reduced the turbidity to 2.58 NTU, corresponding to a removal efficiency of 81.70%, while alum reduced the turbidity to 2.29 NTU, with a removal efficiency of

83.79%. These results further confirm that both coagulants can effectively destabilize suspended particles in peat water.

However, different behavior was observed for sample 3, which had a much lower initial turbidity of 1.34 NTU. After treatment with chitosan, the turbidity slightly increased to 1.55 NTU, resulting in a calculated removal efficiency of −15.30%. This phenomenon may occur when the initial turbidity of the water is already very low. Under such conditions, the addition of polymeric coagulants may lead to incomplete floc formation or the formation of fine suspended particles that remain dispersed in the solution.

In contrast, treatment with alum reduced the turbidity of sample 3 to 0.77 NTU, corresponding to a turbidity removal efficiency of 42.54%. Although the removal efficiency was lower compared with samples 1 and 2, alum still showed measurable turbidity reduction. Overall, the average turbidity removal obtained from the three samples was 49.99% for chitosan and 71.34% for alum, as shown in Table 3. These results indicate that alum exhibited higher overall turbidity removal efficiency compared with chitosan under the experimental conditions used in this study.

The coagulation mechanism of chitosan is mainly attributed to electrostatic interactions between the positively charged sites of chitosan and negatively charged colloidal particles present in water. These interactions promote the formation of larger flocs that can settle more easily (Weiner & Matthews, 2003). However, when the initial turbidity is very low, the distance between suspended particles becomes larger, which may reduce the probability of particle bridging.

Zemmouri et al. (2011) reported that chitosan tends to be less effective in treating water with low turbidity levels. This limitation is related to the bridging mechanism of polymeric coagulants, which requires sufficient particle concentration to form stable flocs. Huang and Chen (1996) also explained that chitosan coagulation primarily occurs through a bridging mechanism, where polymer chains link multiple particles together. Furthermore, Divakaran and Pillai (2001) suggested that floc formation through polymer bridging may require longer sedimentation time to produce larger and more stable flocs. Therefore, the relatively short sedimentation time applied in this study may have contributed to the lower effectiveness of chitosan in some samples.

### *3.4 Removal of Organic Compounds Based on Permanganate Value*

The determination of organic matter content in peat water was carried out using the permanganometric method, which measures the permanganate value as an indicator of oxidizable organic compounds present in the sample. A higher permanganate value indicates a higher concentration of organic substances in the water. The influence of coagulant dosage, pH conditions, and coagulant type on the removal of organic compounds in peat water is presented in Tables 4, 5, and 6, respectively.

#### *3.4.1 Effect of Coagulant Dosage*

The effect of coagulant dosage on organic matter removal is shown in **Table 4**. In contrast, the use of alum resulted in less consistent organic matter removal. The lowest permanganate value obtained using alum was 15.168 mg/L at a dosage of 20 mg/L, corresponding to a reduction of 11.11%. However, this value still exceeded the permissible limit for organic compounds in raw water. In several cases, the permanganate value increased after alum addition, resulting in negative removal percentages.

**Table 4.** Effect of coagulant dosage on organic matter removal (permanganate value)

| Dosage (mg/L) | Chitosan Permanganate (mg/L) | Removal (%) | Alum Permanganate (mg/L) | Removal (%) |
|---|---|---|---|---|
| 5 | 7.90 | 64.29 | 21.804 | -27.78 |
| 10 | 7.90 | 64.29 | 33.812 | -98.15 |
| 15 | 7.90 | 64.29 | 15.484 | 9.26 |
| 20 | 13.272 | 40.00 | 15.168 | 11.11 |
| 25 | 9.796 | 55.71 | 17.38 | -1.85 |

Note: Initial permanganate value = 22.12 mg/L (chitosan) and 17.064 mg/L (alum). According to SNI 01-3553-2006, the maximum permissible organic matter concentration is 10 mg/L.

This phenomenon may be related to the hydrolysis reactions of $Al^{3+}$ ions, which produce various hydroxo complexes such as $Al(OH)^{2+}$, $Al_2(OH)_2^{4+}$, and $Al_3(OH)_4^{5+}$. These reactions may influence the dissociation behavior of humic substances in the solution, potentially causing previously aggregated organic compounds to redisperse. Overall, the results indicate that chitosan exhibited better performance than alum in reducing organic compounds when evaluated based on dosage variation.

### *3.4.2 Effect of pH on Organic Matter Removal*

The influence of pH on organic matter removal is presented in **Table 5**.

**Table 5.** Effect of pH on organic matter removal

| pH | Control (mg/L) | Chitosan (mg/L) | Removal (%) | Alum (mg/L) | Removal (%) |
|---|---|---|---|---|---|
| 5 | 12.5 | 20.856 | -20.00 | 17.696 | 13.85 |
| 6 | 12.7 | 15.168 | 12.73 | 16.116 | 21.54 |
| 7 | 12.5 | 16.116 | 7.27 | 17.38 | 15.39 |
| 8 | 12.8 | 22.12 | -27.27 | 11.376 | 44.62 |
| 9 | 12.0 | 17.38 | 0.00 | 13.272 | 35.39 |

For chitosan, slight reductions in organic matter concentration were observed at pH 6 and pH 7, with removal efficiencies of 12.73% and 7.27%, respectively. Under these conditions, some of the amino functional groups in chitosan remain available to interact with organic molecules present in the peat water. The interaction between chitosan and humic substances may occur through hydrogen bonding and electrostatic interactions between amino groups in chitosan and functional groups present in humic compounds. For alum, the highest organic matter reduction occurred at pH 8, where the permanganate value decreased to 11.376 mg/L, corresponding to a removal efficiency of 44.62%. This behavior may be explained by the formation of aluminum hydroxide precipitates under slightly alkaline conditions. When alum is dissolved in water, hydrolysis reactions produce positively charged hydroxo complexes and eventually form $Al(OH)_3$ flocs, which can adsorb organic compounds present in the water. In alkaline conditions, the presence of hydroxide ions facilitates the formation of these hydrolysis products, thereby enhancing the removal of organic substances. However, it should be noted that

in most experimental conditions, the remaining organic matter concentration after treatment still exceeded the recommended limit of 10 mg/L, indicating that coagulation alone may not be sufficient to completely remove organic compounds from peat water.

### *3.4.3 Effect of Coagulant Type on Organic Matter Removal*

The overall effectiveness of the two coagulants in removing organic compounds was evaluated using three peat water samples, as summarized in **Table 6**.

For chitosan, the average permanganate value obtained after treatment was 13.114 mg/L, corresponding to an average reduction of 4.57%. In contrast, alum produced a lower average permanganate value of 11.903 mg/L, corresponding to a reduction efficiency of 12.27%. These results suggest that alum was relatively more effective than chitosan in reducing organic compounds in peat water. The reduction in organic matter may occur through adsorption of organic molecules onto the flocs formed during the coagulation process.

During alum coagulation, the formation of $Al(OH)_3$ precipitates provides a large surface area that can trap and adsorb organic substances. These flocs subsequently settle during the sedimentation process, thereby reducing the concentration of dissolved organic compounds in the treated water (Suprihanto, 1994).

**Table 6.** Reduction of organic compounds in peat water

| Sample | Treatment | Permanganate Value (mg/L) | Reduction (mg/L) | Removal (%) |
|---|---|---|---|---|
| | Control | 9.796 | 0 | 0 |
| 1 | Chitosan | 7.426 | 2.37 | 24.19 |
| | Alum | 8.374 | 1.422 | 14.52 |
| | Control | 13.588 | 0 | 0 |
| 2 | Chitosan | 15.642 | -2.054 | -15.12 |
| | Alum | 11.692 | 1.896 | 13.95 |
| | Control | 17.064 | 0 | 0 |
| 3 | Chitosan | 16.274 | 0.79 | 4.63 |
| | Alum | 15.642 | 1.422 | 8.33 |

Overall, although both coagulants contributed to the reduction of organic compounds, the results indicate that alum exhibited slightly higher efficiency than chitosan in reducing organic matter based on the permanganate value.

## 4. CONCLUSIONS

This study evaluated the performance of chitosan and alum as coagulants for peat water treatment, with particular emphasis on the effects of coagulant dosage and pH on turbidity and organic matter removal. The results showed that the optimum dosage of chitosan was 5 mg/L, producing a turbidity removal efficiency of 81.91%, while the optimum dosage for alum was 15 mg/L, achieving a turbidity removal efficiency of 76.28%. These results indicate that chitosan requires a lower dosage to achieve effective turbidity reduction compared with alum.

The efficiency of the coagulation process was also influenced by pH conditions. Chitosan exhibited optimum performance at pH 8, while alum showed the highest turbidity removal at pH 7. These findings highlight the importance of controlling pH conditions to optimize coagulation performance during peat water treatment.

In terms of organic matter removal, evaluated through the permanganate value, alum demonstrated slightly higher effectiveness than chitosan. The average reduction in organic compounds obtained using alum was 12.27%, whereas chitosan achieved an average reduction of 4.57%.

Overall, the results suggest that chitosan has potential as an alternative natural coagulant due to its ability to achieve effective turbidity reduction at relatively low dosages, while alum remains more effective in reducing organic matter content in peat water. The combination of operational parameters such as coagulant dosage and pH is therefore essential for optimizing the treatment of peat water.

Further studies are recommended to investigate additional operational parameters, including mixing intensity and sedimentation time, in order to enhance the efficiency of coagulation processes for peat water treatment.

## ACKNOWLEDGMENT

The authors would like to express their sincere gratitude to Universitas Lambung Mangkurat, for the facilities provided to carry out this research. The authors also acknowledge technical assistance and support from all parties who contributed directly or indirectly to the completion of this study.

## LIST OF REFERENCES

Agusnar, H. 2003. Analisa Keefektifan Penggunaan Kitosan untuk Menurunkan Kadar Logam Berat. Jurnal Sains Kimia. 7(1): 7-10.

Amir, R & Isnaniawardhana, J.N. 2008. Penentuan Dosis Optimum Aluminium Sulfat dalam Pengolahan Air Sungai Cileueur Kota Ciamis dan Pemanfatan Resirkulasi Lumpur dengan Parameter pH, Warna, Kekeruhan, dan TSS. Jurnal Program Studi Teknik Lingkungan, Fakultas Teknik Sipil dan Lingkungan Institut Teknologi Bandung.

Anderson, E., L. Darmayanti & Rinaldi. 2013. Pengolahan Air Gambut dengan Media Filter Batu Apung. Jurnal Ilmiah Teknik Sipil UNRI. 1(1): 2-5.

Bachia, M.F. 2006. Gambut: Agroekosistem dan Transformasi Karbon. Yogyakarta: Gadjah Mada University Press.

Budiman, A., C.Wahyudi., W. Irawaty & H. Hindarso. 2008. Kinerja Koagulan Poly Aluminium Chloride (PAC) dalam Penjernihan Air Sungai Kalimas Surabaya menjadi Air Bersih. Widya Teknik. 7(1): 25-34.

Budiyono & Sumardiono. 2013. Teknik Pengolahan Air. Yogyakarta: Graha Ilmu.

Burgess, J., M. Meeker., J. Minton & M. O'Donohue. 2015. International Research Agency Perspectives on Potable Water Reuse. Environmental Science: Water Research & Technology. The royal Society of Chemistry. 5: 563-580.

Campbell, A. 2002. The Potential Role of Aluminium in Alzheimer's Disease. Neprhol Dial transplant. 17(2): 17-20.

Chung, G.H., B.S. Kim., J.W. Hur & H.K. No. 1996. Physicochemical Properties of Chitin and Chitosan Prepared from Lobster Shrimp Shell. Korean Journal Food Science Technology. 28: 870-876.

Crittenden, J.C., R.R Trussell., D.W. Hand., K.J. Howe & G. Tchobanoglous. 2012. MWH's Water Treatment: Principles and Design 3rd Edision. New Jersey: John Wiley and Sons.

Divakaran, R & V.N.S. Pillai. 2001. Flocculation of Kaolinite Suspensions In Water By Chitosan. Wat.Res. 35(1):3904-3908.

Duan, J & J. Gregory. 2003. Coagulation By Hydrolysing Metal Salts.

Ermal, A.S. 2016. Pemanfaatan Precipitated Calsium Carbonate (PCC) dari Limbah Cangkang Kerang Darah (Anadara Granosa) sebagai Adsorben Pengolahan Air Gambut. Skripsi Program Studi Teknik Lingkungan Universitas Riau, Riau.

Goosen, M.F.A. 1997. Application of Chitin and Chitosan. Tecnomic Publishing Company. Inc, Pennsylvania.

Hendrawati., S. Sumarni & Nurhasni. 2015. Penggunaan Kitosan sebagai Koagulan Alami dalam Perbaikan Kualitas Air Danau. Jurnal Penelitian dan Pengembangan Ilmu Kimia. 1(1): 1-11.

Herawati, A., R. Asti, B. Ismuyanto, J. Nanda & A.D.S.N. Hidayati. 2017. Pengaruh pH dan Dosis Koagulan Ekstrak Biji Kelor dalam Koagulasi Terhadap Pengurangan Kekeruhan Limbah Cair. Jurnal Rekayasa Bahan Alam dan Energi Berkelanjutan. 1(1): 25-28.

Hesami, F., B. Bina & A. Ebrahimi. 2014. The Effectiveness of Chitosan as Coagulant Aid in Turbidity Removal from Water. International Journal of Environmental Health Engineering. 2 (6): 46-51.

Howe, K.J., D.W. Hand., J.C. Crittenden., R.R. Trussell & G. Tchobanoglous. 2012. Principle of Water Treatment. John Wiley and Sons, Inc, New Jersey.

Hu, C., H. Liu., J. Qu., D. Wang & J. Ru. 2006. Coagulation Behavior of Aluminum Salts in Eutrophic Water: Significance of Al13 Species and Ph Control. Environmental science & technology. 40(1): 325-331.

Huang, C & Y. Chen. 1996. Coagulation of Colloidal Particles in Water by Chitosan. Journal Chem. Tech. Biotechnol. 66:221-232.

Ismirantie, R., Atmono & T.T. Praja. 2018. Perbandingan Kitosan dari Limbah Udang Windu dan Kitosan Murni Terhadap Penurunan Kadar Besi (Fe) pada Air Sumur Gali. Jurnal Rekayasa, Teknologi, dan Sains. 2 (2): 103-110.

Jana, S., A. Saha., A.K. Nayak., K.K. Sen & S.K. Basu. 2013. Aceclofenac-loaded Chitosan-tamarind Seed Polysaccharide Interpenetrating Polymeric Network Microparticles. Colloids and Surfaces B: Biointerfaces. 105(1): 303–309.

Kalsum, S.U & Indro. 2020. Pemanfaatan Limbah Udang (Kitosan) sebagai Koagulan Alami dalam Penurunan Parameter Air Gambut. Jurnal Daur Lingkungan Hidup. 3(1): 1-4.

Kawamura, S. 1991. Integrated Design of Water Treatment Facilities. John Wiley & Sons, Inc, USA.

Kusnaedi. 2006. Mengolah Air Gambut dan Air Kotor untuk Air Minum. Jakarta: Penebar Swadaya.

Kusnaidi. 2010. Mengolah Air Kotor untuk Air Minum. Jakarta: Swadaya.

Larry, D.B., F.J. Joseph & L.W. Barron. 1982. Process Chemistry for Water and Wastewater Treatment.

Majjid, S.Z & Dernengsih. 2018. Pemanfaatan Kitosan dari Limbah Kulit Udang sebagai Koagulan Penjernih Air. Chemical Process Engineering. 3(1): 27-32.

Manurung, M. 2011. Potensi Kitin/Kitosan dari Kulit Udang sebagai Biokoagulan Penjernih Air. Jurnal Kimia. 5(2): 182-188.

Meicahayanti, I., Marwah & Y. Setiawan. 2018. Efektivitas Kitosan Limbah Kulit Udang dan Alum sebagai Koagulan dalam Penurunan TSS Limbah Cair Tekstil. Jurnal Chemurgy. 2(1): 1-5.

Mu'minah. 2008. Aplikasi Kitosan Sebagai Koagulan untuk Penjernihan Air Keruh. Tesis Program Studi Kimia, FMIPA ITB.

Nastiti, Y., Y. Syarfi & H. Syamsu. 2015. Penyisihan Warna, Zat Organik dan Kekeruhan pada Air Gambut dengan Kombinasi Proses Koagulasi-Flokulasi Menggunakan Koagulan Aluminium Sulfat (AL2(SO4)) dan Membran Ultrafiltrasi. JOM FTEKNIK Unri. 2(2):1-7.

Ozacar, M., & I.A. Sengil. 2003. Evaluation of Tannin as a Coagulant Aid for Coagulation of Colloidal Particles, Colloid and Surfaces A. Physicochem Eng. Aspects. 229: 85 – 96.

Pahlevi, M.R. 2009. Analisis Kadar (Fe) dan Mangan dari Air Gambut Setelah Dijernihkan dengan Penambahan Tulang Ayam. Medan : Pascasarjana – Universitas Sumatera Utara (USU).

Prayudi, T. 2001. Pengaruh Ukuran Partikel Kitosan pada Proses Degradasi Limbah Cair Tektil. Jurnal Teknologi Lingkungan. 2(3):296-299.

Prihatinningtyas, E., & A.J. Effendi. 2013. Aplikasi Koagulan Alami dari Biji

Jagung dalam Pengolahan Air Bersih. Jurnal Tekno Sains. 2(2): 93-95.

Pontius, F.W. 2016. Chitosan as a Drinking Water Treatment Coagulant. American Journal of Civil Engineering. 4: 205-215.

Rathke, T.D & S.M. Hudson. 1994. Review of Chitin and Chitosan as Fiber and Film Formers. Macromol Chem Phys. 34(3): 375-473.

Rao, L.N. 2015. Coagulation and Flocculation of Industrial Wastewater by Chitosan. International Journal of Engineering and Applied Sciences. 2: 50-52.

Rehansyah, M.A., H.S. Edward & S. Elystia. 2017. Penyisihan Zat Organik dan Warna pada Air Gambut dengan Koagulan Alami Campuran (Biji Jagung, Biji Kelor dan Biji Semangka). Jom FTEKNIK. 4(2): 1-9.

Renault, F., B. Sancey., P.M. Badot & G. Crini. 2009. Chitosan for coagulation/flocculation processes – An eco-friendly approach. European Polymer. Journal. 45: 1337-1348.

Rumapea, N. 2009. Penggunaan Kitosan dan Polyalumunium Chlorida (PAC) untuk Menurunkan Kadar Logam Besi (Fe) dan Seng (Zn) dalam Air Gambut. [Tesis]. Universitas Sumatera Utara.

Sinardi., P. Suwondo & Suprihanto. 2013. Pembuatan, Karakterisasi dan Aplikasi Kitosan dari Cangkang Kerang Hijau (Mytulus Virdis Linneaus) sebagai Koagulan Penjernih Air. Teknik Sipil UNS. 2: 5-10.

Soekardi, M & A. Hidayat. 1988. Extent and Distribution of Peat Soils of Indonesia. Dalam paper presented at Third Meeting of the Cooperative Research on Problem Soils.

Suherman, D & N. Sumawijaya. 2013. Menghilangkan Warna dan Zat Organik Air Gambut dengan Metode Koagulasi-flokulasi Suasana Basa. Jurnal Riset Geologi dan Pertambangan. 23(2): 127-139.

Suprihanto. 1994. Pengolahan Air Gambut Kajian Terhadap Studi Labolatorium. Teknik Lingkungan ITB. Bandung.

Suptijah, P., W. Zahiruddin & D. Firdaus. 2008. Pemurnian air sumur dengan kitosan melalui tahapan koagulasi dan filtrasi. Buletin Teknologi Hasil Perikanan. 11(1): 65-72.

Sutrisno, Muhdarina & T.A. Amri. 2014. Pengolahan Air Gambut dengan Koagulasi Cair Hasil Ekstraksi Lempung Alam Desa Cengar Menggunakan H2SO4. JOM FMIPA UNRI. 1(2):13-20.

Trimaily, D., Nofrizal & E. Maryanti. 2017. Efektivitas Penggunaan Tawas dan Tanah Lempung pada Pengolahan Air Gambut menjadi Air Bersih. Dinamika Lingkungan Indonesia. 4(1): 39-52.

Wasisto, S. 1980. Laporan Penelitian Sumber Air Minum dan Cara Pembuangan Kotoran di Daerah Pasang Surut Rantau Rasau Jambi. Pusat Penelitian Ekologi Kesehatan. Badan Litbangkes Depkes RI. Jakarta.

Weiner, R.F & Matthews, R.A. 2003. Enviromental Engineering, Fourth Edision. Elsevier Science, USA.

Yang, Z., B. Gao & Q. Yue. 2010. Coagulation Performance and Residual Aluminium Speciation of Al2(SO4)3 and Polyaluminium Chloride (PAC) in Yellow River Water Treatment. Chemical Engineering Journal. 165: 122-132.

Zadow, R. 2009. The Real Dirth On Humic Subtances. Maximum Yield. 40-44.

Zeijang, 2008.The physical and chemical property of Aluminum sulfat. http://www.chemnet.com/cas/id/10043-013/Aluminumsulfate. html. (Diakses pada tanggal 9 Maret 2021)

Zemmouria, H., S. Kadouche., H. Lounici., M. Hadioui & N. Mameri. 2011. Use of Chitosan in Coagulation Flocculation of Raw Water of Jeddara and Beni Amrene Dams. Water Supply. 11(2): 202-21.